Nano Energy 29 (2016) 65–82

Contents lists available at ScienceDirect

Nano Energy

journal homepage: www.elsevier.com/locate/nanoen

Spectroscopic insights into the nature of active sites in iron–nitrogen–carbon electrocatalysts for oxygen reduction in acid

Qingying Jia [a], Nagappan Ramaswamy [a,b], Urszula Tylus [a], Kara Strickland [a], Jingkun Li [a], Alexey Serov [c], Kateryna Artyushkova [c], Plamen Atanassov [c], Jacob Anibal [d], Cenk Gumeci [d], Scott Calabrese Barton [d], Moulay-Tahar Sougrati [e], Frederic Jaouen [e], Barr Halevi [f], Sanjeev Mukerjee [a,*]

[a] Department of Chemistry and Chemical Biology, Northeastern University, Boston, MA 02115, United States
[b] Global Fuel Cell Activities, General Motors Corporation, Pontiac, MI 48340, United States
[c] Department of Chemical & Biological Engineering, Center for Micro-Engineered Materials (CMEM), The University of New Mexico, Advanced Materials Laboratory, Albuquerque, NM 87106, United States
[d] Department of Chemical Engineering and Materials Science, Michigan State University, East Lansing, MI 48824, United States
[e] Institut Charles Gerhardt Montpellier, UMR CNRS 5253, Université Montpellier, Agrégats, Interfaces et Matériaux pour l'Energie, Montpellier 34095, France
[f] Pajarito Powder, LLC (PPC), Albuquerque, NM 87102, United States

ARTICLE INFO

Article history:
Received 17 February 2016
Received in revised form
25 March 2016
Accepted 30 March 2016
Available online 6 April 2016

Keywords:
Oxygen reduction
Non-platinum group catalyst
Active site
In situ XAS, redox catalysis

ABSTRACT

Developing efficient and inexpensive catalysts for the sluggish oxygen reduction reaction (ORR) constitutes one of the grand challenges in the fabrication of commercially viable fuel cell devices and metal–air batteries for future energy applications. Despite recent achievements in designing advanced Pt-based and Pt-free catalysts, current progress primarily involves an empirical approach of trial-and-error combination of precursors and synthesis conditions, which limits further progress. Rational design of catalyst materials requires proper understanding of the mechanistic origin of the ORR and the underlying surface properties under operating conditions that govern catalytic activity. Herein, several different groups of iron-based catalysts synthesized via different methods and/or precursors were systematically studied by combining multiple spectroscopic techniques under ex situ and in situ conditions in an effort to obtain a comprehensive understanding of the synthesis-products correlations, nature of active sites, and the reaction mechanisms. These catalysts include original macrocycles, macrocycle-pyrolyzed catalysts, and Fe−N–C catalysts synthesized from individual Fe, N, and C precursors including polymer-based catalysts, metal organic framework (MOF)-based catalysts, and sacrificial support method (SSM)-based catalysts. The latter group of catalysts is most promising as not only they exhibit exceptional ORR activity and/or durability, but also the final products are controllable. We show that the high activity observed for most pyrolyzed Fe-based catalysts can mainly be attributed to a single active site: non-planar Fe–N_4 moiety embedded in distorted carbon matrix characterized by a high potential for the $Fe^{2+/3+}$ redox transition in acidic electrolyte/environment. The high intrinsic ORR activity, or turnover frequency (TOF), of this site is shown to be accounted for by redox catalysis mechanism that highlights the dominant role of the site-blocking effect. Moreover, a highly active MOF-based catalyst without Fe–N moieties was developed, and the active sites were identified as nitrogen-doped carbon fibers with embedded iron particles that are not directly involved in the oxygen reduction pathway. The high ORR activity and durability of catalysts involving this second site, as demonstrated in fuel cell, are attributed to the high density of active sites and the elimination or reduction of Fenton-type processes. The latter are initiated by hydrogen peroxide but are known to be accelerated by iron ions exposed to the surface, resulting in the formation of damaging free-radicals.

* Corresponding author.
E-mail address: s.mukerjee@neu.edu (S. Mukerjee).

http://dx.doi.org/10.1016/j.nanoen.2016.03.025
2211-2855/

Contents

1. Introduction

The stability criterion has hitherto restricted the range of suitable materials for accelerating the sluggish oxygen reduction reaction (ORR) in acidic environment to noble metals such as Pt and Pt-alloys. Overcoming this limitation has been the cornerstone of materials design and discovery for electrochemical energy conversion devices such as proton exchange membrane fuel cells (PEMFCs) and metal–air batteries. The replacement of unsustainable noble-metal catalysts with abundant and inexpensive materials has attracted much research attention and recently witnessed important progress. Specifically regarding the development of non-platinum group metal (non-PGM) catalysts for the ORR, research conducted over the past five decades has investigated a broad variety of materials, including heme-centered analog macromolecules such as metal-phthalocyanines or -porphyrins [1,2], nitrogen-functionalized graphene-based materials (N–C, M–N–C, with M=Fe, Co) [3,4], chalcogenide [5–9] and metal oxides [10–12]. Among these candidates, M–N–C materials are most promising since their beginning-of-life ORR activities now approach those of Pt/C reference materials in acidic electrolyte [3,4,13,14]. Despite these achievements, current synthetic routes and the interpretation of material's properties primarily rely on empirical trial-and-error combinations of precursors and synthesis conditions, owing to the uncertainty over the exact nature of active sites in M–N–C materials, and over the way the ORR kinetics is mediated by these sites. Substantial improvements in both activity and durability, which is essential for the successful implementation of M–N–C catalysts in fuel cells, will require proper understanding of the mechanistic origin of the ORR and of the underlying surface properties that govern catalytic activity in such materials.

1.1. Synthesis methods

Cobalt phthalocyanine (CoPc) was first demonstrated to be ORR active in alkaline conditions by Jasinski in 1964 [1]. In the 1970s, a first breakthrough was realized with the discovery that pyrolyzing M–N_4 macrocycle samples in inert gas resulted in materials with substantially increased durability and/or activity [15–17]. In 1989, Yeager et al. [18] demonstrated that M–N–C materials with high ORR activity can also be prepared via the pyrolysis of a catalyst precursor based on a simple iron salt and a nitrogen-rich polymer. This finding provided more flexibility in the preparation of catalysts and range of potential M, N and C precursors, including precursors with much lower-cost than the molecular M–N_4 macrocycles. Since then, M–N–C catalysts have been prepared from a wide variety of precursors using different procedures to synthesize, mix or pyrolyze catalyst precursors, in an effort to create non-PGM catalysts with ORR activity and durability competing those of Pt in acidic pH electrolyte [3,4,13,14,19,20]. In the meanwhile, studies on M–N_4 macrocycles have also progressed in both practical and fundamental aspects [21–24].

Ultimately, high performance Fe-based catalysts have been achieved via different synthesis methods involving different precursors. In 2009, Dodelet's group developed a Fe-based catalyst that displays a volumetric activity of 98 A cm^{-3} at an iR-free cell voltage of 0.8 V [4]. This catalyst was derived from the NH_3 pyrolysis of a catalyst precursor comprising a Fe salt, phenanthroline and a high-surface-area carbon powder (Black Pearls 2000). The activity was significantly increased to 230 A cm^{-3} at an iR-free cell voltage of 0.8 V by replacing Black Pearls 2000 with a specific MOF, namely zeolitic-imidazolate-framework 8 (ZIF-8) [20]. The enhanced activity was attributed to the much higher BET area of the highly porous MOF and resulting catalyst, and/or to the creation of a new active site in which the central Fe is off the N_4 plane [25]. It is known from studies on synthetic heme-like and biological heme-based macrocycles that the presence of a fifth ligand occupying the axial position can pull the Fe ion out of the N_4 plane [21,26]. In Mössbauer spectroscopy studies, this site has been labeled D3, referring to a quadrupole doublet component with high isomer shift in the Mössbauer spectra [25]. Since then, a great deal of work has been devoted to the further advancement and understanding of MOF-derived catalysts. Most recently, a MOF-derived Fe–N–C catalyst free of inorganic Fe species developed by Zitolo et al. [13] exhibited an apparent ORR activity surpassing that of a commercial Pt/C catalyst in 0.1 M $HClO_4$ electrolyte in rotating disk electrode (RDE). While the active sites were proposed to be porphyrinic moieties in highly disordered graphene sheets and/or between zigzag graphene edges, the authors stated that the exceptional intrinsic ORR activity of the catalytic sites is not exclusively set by the local geometry of the active sites but also tuned by the high basicity of the N-doped carbon. The latter is typical for NH_3-pyrolyzed materials. In parallel, we recently developed another type of MOF-derived catalyst characterized by active sites that are devoid of any direct nitrogen coordination to isolated iron ions and that outperforms the benchmark platinum based catalyst in alkaline media, and is comparable to its best M–N–C contemporaries in acidic media [14]. These studies highlight the general interest in using MOFs as a platform of sacrificial materials to prepare M–N–C catalysts exhibiting state-of-art ORR activity and decent durability, and reveal how the nature of the active sites in the final pyrolytic products is now controllable

through the structure and distribution of the metal-organic and iron-salt precursors and pyrolysis conditions.

In the meanwhile, great progress was also achieved in developing M–N–C catalysts derived from inorganic metal salts, nitrogen-containing compounds and a carbon support. Wu et al. reported polyaniline Fe (PANI-Fe-C) and FeCo (PANI-FeCo-C) catalysts that show a power density of 550 mW cm^{-2} in PEMFC [3]. These PANI-derived catalysts have an onset potential of ~0.93 V vs. the reversible hydrogen electrode (RHE) in fuel cell, which is higher than that reported for previous non-PGM catalysts with onset potentials ranging from 0.80 to 0.85 V [27]. In addition to its promising ORR activity, PANI-FeCo-C catalysts also exhibited relatively high durability (700 h) at 0.4 V in fuel cell [3].

Recently, a series of highly active and durable Fe–N–C catalysts was also successfully synthesized from a catalyst precursor involving a ferrous salt and a nitrogen-containing charge-transfer salt with the open-frame structure controlled by the sacrificial silica-templating synthesis method (SSM) [19,28]. A cathode comprising 4 mg cm^{-2} of the best SSM-catalyst reached a current density of *ca* 100 mA cm^{-2} at an iR-free cell voltage of 0.8 V. In addition, this catalyst presented a minimized drop of the half-wave potential of only 3–4% relative to the initial value using the DOE Durability Working Group (DWG) proposed protocol and Nissan load-cycling protocol in RDE tests [29].

1.2. Active-site structure hypotheses

Despite these clear-cut progresses in developing M–N–C catalysts, the exact nature of the active sites induced by high temperature pyrolysis still remains unclear, and even more so the detailed reaction mechanisms occurring on such sites during ORR. The respective role of the M, N, and C elements toward the formation of ORR active sites at high temperature has been under intensive debate since 1989, although it is acknowledged that all these elements are simultaneously required either in the starting catalyst precursor or during at least one pyrolysis step (N might be absent from the catalyst precursor but introduced during pyrolysis as a gas) in order to produce ORR catalysts that are efficient in acidic media. Regarding the role of the transition metal M, many researchers believe that it constitutes the core of the active site and directly participates in the ORR, as is the case for non-pyrolyzed macrocycles [13,21–25,30,31]. In a large study involving more than forty M–N–C electrocatalysts, structure–property relationships between surface speciation determined by X-ray Photoelectron Spectroscopy (XPS) and electrochemical performance have demonstrated that iron coordinated to nitrogen is an active site for $4e^-$ direct reduction of O_2 to H_2O [32]. Using aberration-corrected annular dark field scanning transmission electron microscopy (STEM-ADF) and electron energy loss spectroscopy (EELS) mapping techniques, Li et al. [33] directly observed the iron atoms on the edge of graphene sheets in close proximity to nitrogen species. This provided a visual experimental evidence for the existence of FeN_xC_y moieties in pyrolyzed materials, an aspect that many synthetic chemists were reluctant to even consider possible. The direct involvement of Fe in catalyzing the ORR was further demonstrated for several Fe-based catalysts in some of our recent studies [21,30]. In situ and operando spectroscopic studies have shown that the Fe^{3+} to Fe^{2+} redox transition, occurring when scanning the electrode potential negatively, is accompanied by the desorption of oxygenated species from the central Fe ion, the Fe^{3+}/Fe^{2+} redox potential being closely related to the ORR onset potential. Further proving the direct involvement of Fe, the ORR activity of Fe–N–C catalysts drop significantly when contacted by cyanide ions, which has been interpreted as a poisoning effect (strong coordination) of CN^- on the Fe-based active sites, a phenomenon occurring on well-defined Fe-based macrocycles as well [30,34]. Among all 3d transition metals from the first row from Cr to Cu, Fe-based catalysts have exhibited the highest ORR activity. While the durability of Fe–N–C catalysts is not yet sufficient, it was shown to be significantly enhanced by mixing Co with Fe [3].

Besides MN_xC_y surface moieties, metallic particles or metal oxide/carbide/nitride particles encapsulated in N-doped carbon shells (denoted as M@N-C hereafter) simultaneously formed during the heat treatment may partly or entirely (depending on specific samples) be responsible for the overall ORR activity [14,35,36]. Specifically, it was proposed that the simultaneous presence of MN_xC_y moieties and M@N-C species in certain catalysts is essential for a high onset-potential in acidic environment [30,37]. This might be accounted for by the dual-site mechanism whereby two adjacent sites, i.e. one MN_xC_y moiety and one M@N-C particle, are required to efficiently promote the $4e^-$ reduction pathway [30,37]. This dual-site mechanism is questioned by recent studies showing that some Fe–N–C catalysts devoid of any M@N-C species also exhibit high ORR activities and near $4e^-$ pathway in acidic media [13,38]. While these studies demonstrate that FeN_xC_y moieties ($x=4$, most likely) with slightly different local configurations resulting in different Mössbauer doublet signatures are efficient sites for the ORR, by no means do they exclude the possibility that certain M@N-C structures are ORR-active as well. In order to conclude on the latter possibility, the preparation of M–N–C materials that exclusively comprise M@N-C species (devoid of MN_xC_y moieties) will be required. Indeed, it was demonstrated by many groups that metallic Fe encapsulated in carbon nanotubes [36] or graphitic layers [14,35] can serve as a new active site for the ORR, even in acidic media [39], and that carbon-encapsulated metallic Fe indirectly facilitates the ORR via modification of the electronic properties of the surface carbon layer. Similarly, Chung et al. [40] showed that PtFe nanoparticles encapsulated in thin N-doped carbon shells (~1 nm) are highly active and durable for ORR, whereas the ones with thick carbon shells (~3.5 nm) are inactive. The concept of reactivity for M@N-C structures has also been extended for hydrogen evolution in acid medium, with nanoparticles of metallic Fe encapsulated in 1–3 graphene layers exhibiting high activity and stability [41]. These studies suggest that the ORR activity of M–N–C catalysts comprising M@N-C structures is very sensitive to the thickness of the N-doped carbon shell surrounding such structures, explaining why the ORR activity of M@N-C structures may vary drastically among non-PGM catalysts prepared via different routes. In addition, Guo et al. [42] demonstrated most recently the non-negligible ORR activity of pyridinic nitrogen-doped carbon in acid medium. These new findings further broaden the possibilities for active sites and complexity in disentangling the overall ORR activity and stability of M–N–C materials, given that N_xC_y sites are always present in such materials, while either MN_xC_y moieties and/or M@N-C particles also co-exist in pyrolyzed non-PGM catalysts.

On the other hand, other researchers have argued that the transition metal only serves to catalyze the formation of special N_xC_y active sites during the pyrolysis procedure rather than being part of the active sites existing in M–N–C materials. In this view, the ORR activity is exclusively attributed to metal-free N_xC_y sites [43,44]. This concept may however overlap with that of the active sites labeled M@N-C, where the metal is a subsurface element, probably not in direct contact with O_2 or the electrolyte during operation. Regarding the true ORR activity of completely metal-free N–C materials in acid medium, reaching a consensual answer has often been obscured by the presence of rather large or, at best, trace content of metal in most studied samples. Many previously claimed 'metal-free' N–C catalysts with decent or high ORR activity were in fact synthesized with Fe-containing precursors, or the authors did not carefully check if the resulting material was free of trace amount of metal [45,46]. It is highly debatable that this class

of catalysts is "metal-free" since Fe impurities from Fe-containing precursors cannot be completely removed by post-pyrolysis acidic treatment [47], especially when Fe is encapsulated in carbon. Moreover, trace amount of iron may be inadvertently introduced when using supposedly iron-free chemicals, or introduced during the preparation (milling or mixing procedure with stainless steel equipment). Residual Fe impurities, even at trace amounts (<200 ppm) that are undetectable by regular elemental analysis techniques such as X-ray photoelectron spectroscopy (XPS) and energy-dispersive X-ray spectroscopy (EDX), can greatly promote the ORR [48,49]. As a minimum safeguard, it has been suggested by Schumann et al. [50] that any sample synthesized using a Fe-containing precursor shall not be classified as a "metal free" N–C catalyst. In addition, Fe impurities may also come from many other sources such as the KOH electrolyte that is commonly used for RDE testing, which was demonstrated to significantly promote the oxygen evolution reaction (OER) [51]. Therefore, even for N–C catalysts synthesized without using Fe-containing precursors, proper poisoning tests with appropriate poisoning probes such as CN^- ions (note that CO is an invalid metal-poisoning probe since it poisons neither unpyrolyzed macrocycles nor pyrolyzed Fe-based catalysts in RDE at room temperature [52]) are necessary to justify the complete absence of metal on the top-surface. In general, the ORR activity of unadulterated metal-free N–C catalysts in acidic media is far inferior to the counterpart M–N–C catalysts [32,42,49]. As mentioned earlier, the intrinsic activity of surface N_xC_y moieties may however be increased by subsurface metal structures.

In contrast to the debate on the role of the metal, the paramount importance of nitrogen to reach high ORR activity for both N–C and M–N–C materials is undisputed. While the incorporation of nitrogen has been demonstrated indispensable for ORR activity, the exact nitrogen type that is most active toward ORR (or toward binding Fe in FeN_xC_y moieties) is still a controversial topic. The nitrogen atoms that are directly bonded to the central Fe in the original macrocycles such as iron phthalocyanines and iron porphyrins are pyrrolic. Using Mössbauer spectroscopy, the active site FeN_4C_y in low spin-state (commonly labeled as D1) has been identified across research groups around the world in both Fe-macrocycle-pyrolyzed catalysts [24,31,53] and Fe–N–C materials synthesized from individual Fe, N, and C precursors [13,19,23,25]. It was first hypothesized that this site features a $Fe–N_4$ core with 2 pyridinic N atoms from the armchair edge of one graphene sheet, and 2 other pyridinic N atoms from the armchair edge of another (facing) graphene sheet, the edges of the two graphene sheets defining a micropore [4]. This structure is consistent with the findings that (i) microporous surface area is important to reach a high density of active sites [14,23,25], (ii) pyridinic nitrogen is selectively formed on the edge of carbon sheets [54], and (iii) a higher relative content of $N_{pyridinic}$ often correlates with better ORR activity [55,56]. However, Jaouen et al. [13] recently argued, based on advanced X-ray absorption near edge structure (XANES) analysis, that this site is formed via an unusual integration of the FeN_4 moiety with pyrrolic N in the bridging edges of graphitic pores or zigzag graphene edges (porphyrinic structure). In this analysis, the nitrogen atoms binding the central iron ion are structurally pyrrolic (i.e. included in a five-membered ring), but they may still be chemically-speaking pyridinic (i.e. sharing $1e^-$ in the delocalized π system of the aromatic ring and having a lone pair of electrons, important to coordinate Fe). While the XANES analysis is highly sensitive to the spatial arrangement of N and C carbons around the central Fe atom, it is poorly sensitive to the coordination state of these light elements. Besides these FeN_4C_y moieties with four coordinated nitrogen atoms, FeN_3 [57] and X-FeN_4 moieties (X representing an axial ligand) [21,25,58,59] integrated in graphene sheets were recently shown to be possible alternative active sites with high ORR activity in pyrolyzed Fe-based catalysts.

The porous structure and electronic properties of carbon are other critical factors for the ORR activity of M–N–C materials. Ramaswamy et al. [22] reported that highly disordered carbon supports yield higher ORR turnover numbers for FeN_4 moieties (intrinsic activity of the moiety). This was explained on the basis of the electron-withdrawing character of carbon and its ability to optimize the bond strength between the metal center and the ORR intermediates. More recently, Jaouen et al. [13] stated that the superior intrinsic ORR activity of NH_3-pyrolyzed Fe–N–C materials relative to that of Ar-pyrolyzed Fe–N–C materials shall be attributed to the much higher basicity of the N-doped carbon after NH_3 treatment, rather than the local geometry of the active sites. In spite of a factor 30 ratio in ORR activity, The XANES, EXAFS and Mössbauer signatures of the FeN_xC_y moieties were indeed nearly identical for Ar- or NH_3-pyrolyzed materials. These studies show that the concept of turnover frequency, even for a given FeN_xC_y moiety, is insufficient to describe the activity of such sites, with longer distance interaction with the carbon matrix also largely tuning the turnover frequency of any specific site structure.

Compiling all the discussions above, it becomes apparent that all the M, N, and C elements play important roles affecting the catalytic activity of M–N–C and M@N-C catalysts, and most likely it is the complicated interplay within these elements that governs the overall catalytic activity. Ideally, a full characterization of all the factors under working conditions can lead to rational design of this group of catalysts, but a more realistic way is to find the underlying descriptors that govern the ORR activity, which requires proper understanding of the ORR kinetics.

1.3. ORR mechanism hypotheses

Due primarily to the different opinions on the nature/structure of the active sites, various ORR pathways have been proposed such as the direct $4e^-$ reduction, [3,4,60] $2e^-$ reduction, [61,62], $2+2e^-$ peroxide pathway on a single site, or $2\times 2e^-$ peroxide pathway on two sites (dual-site mechanism) [30,37,63]. The ideal ORR kinetics with the highest efficiency in power generation and minimized risk of peroxide release is the reduction of O_2 to H_2O via a direct four-electron ($4e^-$) pathway mediated by a single site. A consensus that FeN_xC_y centers can efficiently promote the direct 4e-reduction of O_2 appears to be reached lately as some Fe–N–C catalysts without any M@N-C species exhibit exceptional ORR activity, and as low % H_2O_2 as measured for Pt/C catalysts (1–3%) [13,38]. In addition, a direct correlation between the content of FeN_xC_y centers and the kinetic current density of ORR has been observed based on both XPS and ^{57}Fe Mössbauer spectroscopy results [23–25,53,56]. More recently, the M@N-C sites have also been shown to efficiently perform either the direct $4e^-$ reduction or $2+2e^-$ reduction (not distinguishable with RRDE) in acidic media. The absence of FeN_xC_y centers in those catalysts was justified either by lack of CN^- poisoning or by in situ XAS method [14,35,36,39]. Therefore, it is not surprising that a dual-site 2×2 mechanism has been proposed for catalysts containing both FeN_xC_y and M@N-C species, whereby oxygen is first reduced to H_2O_2, desorbed and then readsorbed on a second site to be further reduced to H_2O [22,30,37,63]. This process may also occur in parallel with a direct 4e reduction, depending on the probability of OOH intermediates to desorb from specific active sites before being reduced to water. Through systematic spectroscopic and electrochemical characterization of more than 40 different metal free and Fe–N–C composites, the role of multiple types of sites in ORR has been established in Atanassov et al.'s recent publication: [56] pyrrolic nitrogen catalyzes the first step of oxygen reduction to hydrogen peroxide; pyridinic nitrogen serves as a second step of hydrogen peroxide reduction to water; and $Fe–N_x$ centers catalyze

4e-direct reduction of oxygen to water and/or the second step of hydrogen peroxide reduction similarly to the pyridinic nitrogen.

As the catalytic role of M@N-C species is still under debate, here we focus primarily on the ORR kinetics mediated by FeN_xC_y centers. Based on in situ XAS studies on several representative Fe–N_x–C catalysts, we recently showed that the ORR process is mediated by the reversible $Fe^{2+/3+}$ redox transition [21], and the population of the catalytically active sites and the reaction rate can be expressed as

$$N_{active}=N_{total}\frac{1}{1+e^{\frac{F}{RT}(E-E_{redox})}} \quad (1)$$

$$\Theta_{O^*}=\frac{N_{total}-N_{active}}{N_{total}}=\frac{1}{1+e^{-\frac{F}{RT}(E-E_{redox})}} \quad (2)$$

$$J\propto N_{total}(1-\Theta_{O^*})\exp\left(-\frac{\Delta H^*}{RT}\right)\exp\left(-\frac{E-E^0}{b}\right) \quad (3)$$

where J is the kinetics current density obtained at the applied potential E. N_{active} and N_{total} are the available (adsorbate free) and total number of surface active sites, respectively; F is the Faraday constant; R is the universal gas constant; T is the temperature; E_{redox} is the redox potential under the relevant operation conditions; Θ_{O^*} is the coverage by adsorbed oxygen species at potential E; ΔH^* is the activation entropy for the electrocatalytic process; E^0 is the standard potential for the Faradaic process; and b is the value of the Tafel slope.

The validity of the redox mechanism for Fe–N–C catalysts is justified by the pre-exponential factor $(1-\Theta_{O^*})$, which indicates that the activity is proportional to the fraction of unoccupied active sites at the applied potential. Since Θ_{O^*} as a function of E exhibits a sharp decrease below E_{redox} (Eq. (2)), decent ORR activity at a fixed potential E can only be observed if the value for E_{redox} of an active site is not much lower than E. Considering a redox potential of 0.7 V and E=0.8 V vs. RHE, a potential typically used for non-PGM catalyst activity evaluation, 98% of the active sites are poisoned by oxygen adsorbates at this target potential. In contrast, considering E_{redox}=0.9 V and E=0.8 V, only 2% of the active sites are then predicted to be occupied by oxygen adsorbates. Thus active sites with redox potentials below 0.7 V are nearly inactive at high potential while an anodic shift of the redox potential from 0.7 V to 0.9 V leads to an activity enhancement of a factor of 49 if only considering the site-blocking effect. This site-blocking effect plays a dominant role for the ORR activity of FeN_xC_y centers given that their redox potentials are mostly below 0.8 V in acidic media [3,21,22,30,52,64]. This effect has been largely overlooked since its proper evaluation requires in situ measurements of oxygen-adsorbate coverage under operating conditions, a challenging experiment recently achieved by us using in situ XAS, further exposed below [21].

By far, most investigations focusing on the active sites of M–N–C catalysts are based on ex situ physicochemical characterization such as Mössbauer spectroscopy [25,65,66], X-ray photoelectron spectroscopy (XPS) [25,53,67], X-ray diffraction (XRD) [68,69], time of flight secondary-ion mass-spectroscopy (ToF-SIMS) [70,71] or transmission electron microscopy (TEM) [3,72,73]. However, such information may be disconnected from the electrocatalysis process as we recently showed that the local structure of the FeN_xC_y moieties under in situ conditions is different from that under ex situ conditions. The local structure was shown to drastically change during ORR, induced by the $Fe^{2+/3+}$ redox transition, as revealed with advanced in situ XAS studies [21]. In this work, a broad variety of pyrolyzed Fe–N–C catalysts were systematically investigated by combining in situ XAS and ex situ Mössbauer spectroscopy to elucidate the structure/activity correlations within Fe-based catalysts.

The present paper now critically reviews earlier works that focused on the nature of the active sites in M–N–C catalysts and also presents new experimental results on diverse Fe–N–C materials representative of the entire class (samples comprising exclusively FeN_xC_y moieties, or exclusively M@N-C species or hybrid materials comprising both types of active sites) obtained from combined ex situ and in situ Mössbauer and XAS results, respectively. The results are discussed and their implications toward an improved general understanding of the detailed ORR mechanisms in such materials exposed.

2. Results and discussion

2.1. Macrocycle-based Fe–N–C catalysts

To elucidate the nature of the active sites formed upon pyrolysis of macrocycles with pre-existing square-planar $Fe–N_4$ moieties as well as the structural origin of their enhanced ORR activity compared to that of the parent macrocycles, we selected a representative iron porphyrin, namely chloro-tetraphenylporphyrin, FeTPPCl. The latter was dispersed on carbon and pyrolyzed at various temperatures and subsequently investigated with ex situ XPS, in situ XAS and rotating disk electrode (RDE) methods. As shown in Fig. 1, the activity of FeTPPCl-pyrolyzed catalysts acquired in 0.1 M $HClO_4$ increases with increasing pyrolysis temperature up to 800 °C. Further increase of the pyrolysis temperature reduced the ORR activity, and is explained by the major presence of inactive metallic iron and/or iron oxides in the final products [22]. The activity enhancement induced by pyrolysis up to 800 °C was ascribed to the drastic anodic shift of the $Fe^{2+/3+}$

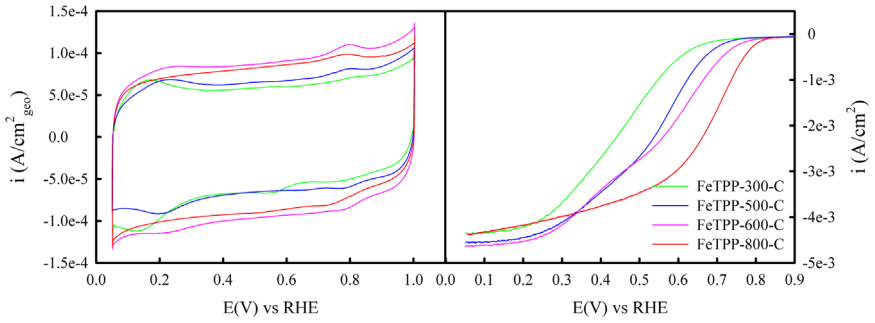

Fig. 1. (a) Cyclic voltammograms (CV) of the FeTPP-pyrolyzed catalysts measured in N_2-purged 0.1 M $HClO_4$ at a scan rate of 20 mV s^{-1} and (b) ORR voltammograms of the catalysts measured in O_2-purged 0.1 M $HClO_4$ at 900 rpm rotation rate and 20 mV s^{-1} scan rate. Reproduced with permission from Ref. [21]. Copyright 2015, American Chemical Society.

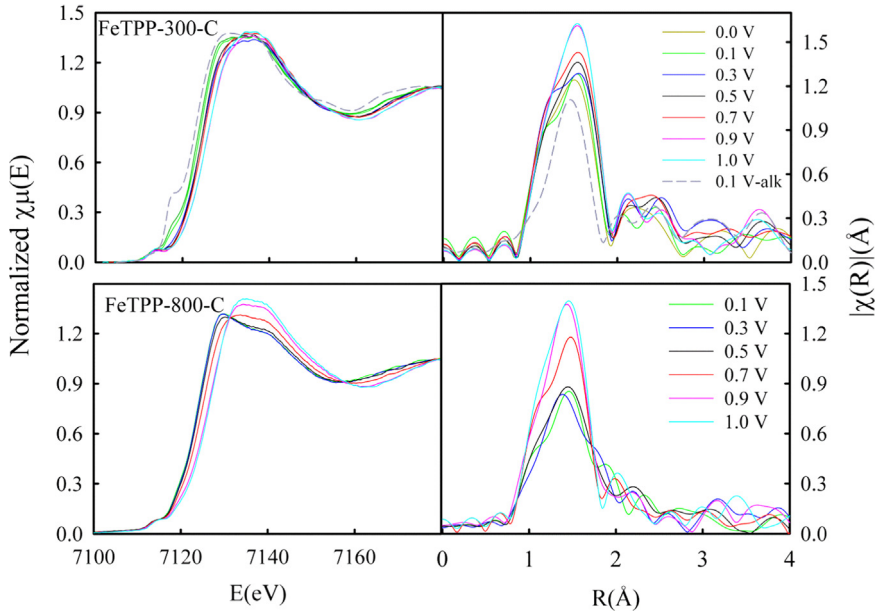

Fig. 2. XANES (left) at the Fe K-edge and the corresponding FT-EXAFS (right) of FeTPP-300-C (top) and FeTPP-800-C (bottom) as a function of applied potential. The spectra were collected in N_2-saturated 0.1 M $HClO_4$ electrolyte. The spectrum of FeTPP-300-C collected at 0.1 V in N_2-saturated 0.1 M KOH electrolyte is also included here as a reference of this catalyst with Fe in +2 oxidation state. Reproduced with permission from Ref. [21]. Copyright 2015, American Chemical Society.

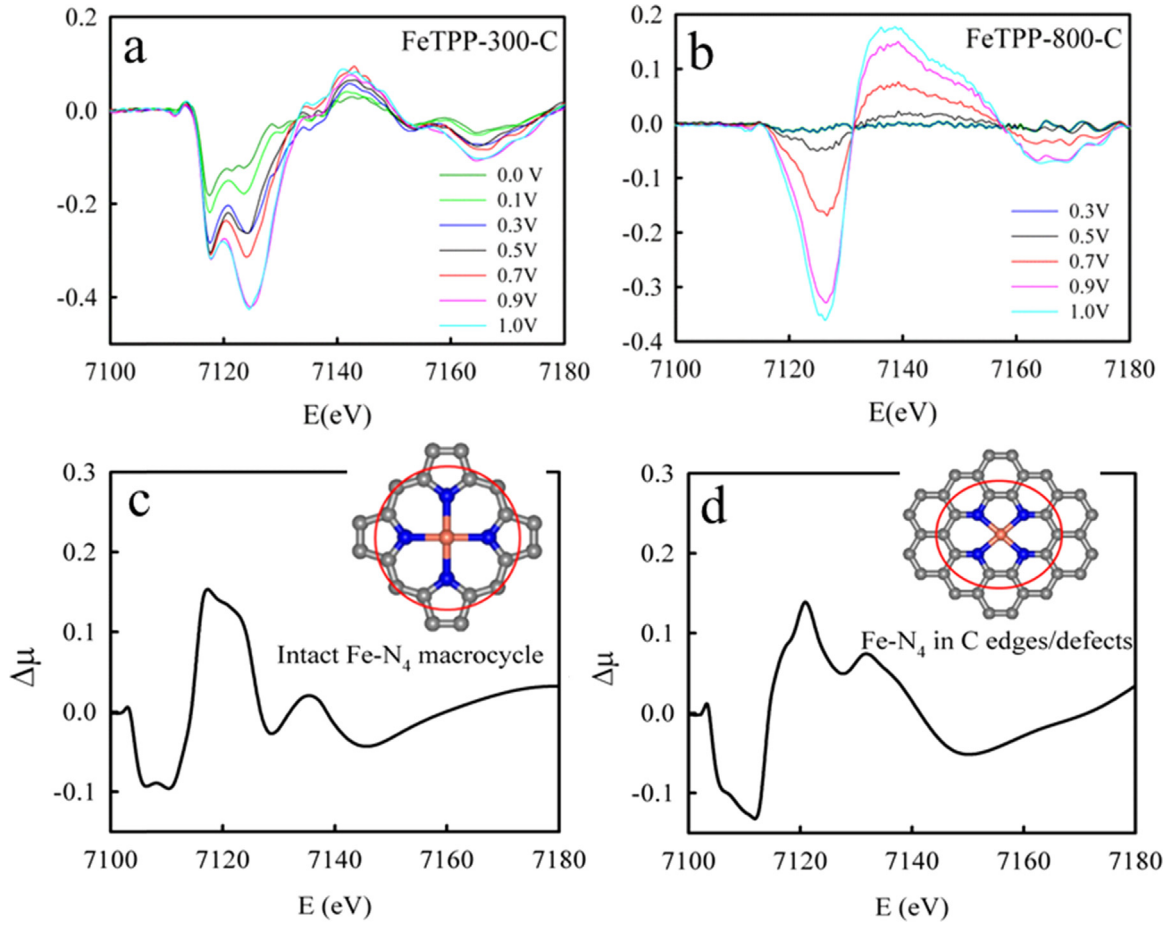

Fig. 3. In situ Fe K-Edge Δμ spectra of FeTPP-300-C (a) and FeTPP-800-C (b) in O_2-saturated 0.1 M $HClO_4$ electrolyte under various potentials. Δμ spectra recorded at a given potential in N_2-saturated electrolyte were identical to those measured under O_2 saturation, within experimental error. Structural models shown in the insets of panels c and d were utilized for Δμ analysis using FEFF9 simulation. Color codes in structural models: orange, iron; blue, nitrogen; gray, carbon. Reproduced with permission from Ref. [21]. Copyright 2015, American Chemical Society.

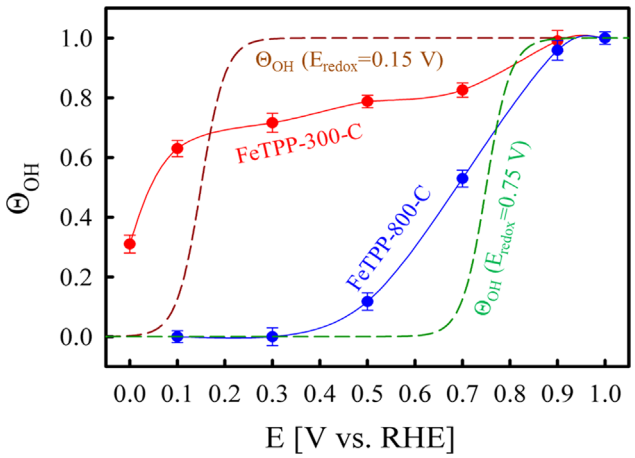

Fig. 4. Experimental values of Θ_{OH}(s) for FeTPP-300-C and FeTPP-800-C as a function of potential extracted from the Δμ data, in comparison to the two calculated Θ_{OH}(s) functions based on Eq. (2) using the redox potential of 0.15 V or 0.75 V, respectively, and the temperature of 298 K. Reproduced with permission from Ref. [21]. Copyright 2015, American Chemical Society.

redox potential from ~0.15 V to ~0.75 V (Fig. 1a) (all the applied potentials in this work are versus reversible hydrogen electrode (RHE) without otherwise stated) [22], which greatly minimizes the site-blocking effect [21,74] by stabilizing the $Fe^{2+}N_4C_y$ active sites at elevated potentials. This redox mechanism is further confirmed by in situ XAS that closely monitors the oxidation state of the Fe ions as a function of applied potentials and the associated changes in local coordination environment. As can be seen in Fig. 2, the Fe K-edge for the catalysts pyrolyzed at 300 and at 800 °C shifts toward higher energy with increasing potential from 0.1 to 1.0 V, indicating the Fe^{2+}/Fe^{3+} redox transition [21,22,75]. Concurrently, the Fourier transform (FT) peak at ~1.6 Å (distance without phase correction) arising from the Fe–N/O scattering increases in intensity, denoting the increase in coordination numbers. These combined results point to the Fe^{2+}/Fe^{3+}redox transition associated with the adsorption of OH* through water activation:

$$N_4\text{–}Fe^{2+} + H_2O \rightarrow N_4\text{–}Fe^{3+}\text{–}OH_{ads} + H^+ + e^- \quad (4)$$

The extent of the OH_{ads} coverage on the FeN_xC_y sites is quantitatively represented by the Δμ magnitude ($|\Delta\mu|$) of the negative dip centered at 7126 eV as a function of potential (Fig. 3). The increase in $|\Delta\mu|$ with increasing potential up to 1.0 V indicates that the Fe^{2+}-sites are progressively occupied by OH_{ads} until reaching occupancy saturation at 1.0 V. The relative OH_{ads} coverage (Θ_{OH}) at a potential E may thus be estimated by the ratio $|\Delta\mu_E|/|\Delta\mu_{1.0\ V}|$. The experimental dependence of Θ_{OH} with electrochemical potential for FeTPP-300-C and FeTPP-800-C is presented in Fig. 4 as solid curves while the theoretical dependence of Θ_{OH} as predicted from Eq. (2) and with values of the redox potential of 0.15 V or 0.75 V (The redox observed for FeTPP-300-C and FeTPP-800-C) are also included for comparison (dashed curves). As clearly seen, the Θ_{OH} coverage for FeTPP-800-C is much lower than that for FeTPP-300-C over the entire potential range, as a result of the higher $Fe^{2+/3+}$ redox potential of the former.

A more comprehensive understanding of the anodic shift of the $Fe^{2+/3+}$ redox potential induced by pyrolysis of macrocycles was acquired by combining the XPS study at the carbon edge and in situ XAS study at the Fe K-edge. We previously showed that the full-width at half maxima (fwhm) of carbon-1s photoemission spectra of pyrolyzed-FeTPP catalysts positively correlates with the $Fe^{2+/3+}$ transition potentials, and also linearly correlates to the ORR turnover numbers of FeN_4 moieties [22]. We accordingly proposed that the pyrolysis relocates the Fe–N_4 active site from a π-electron-rich macrocyclic ligand environment to a relatively π-electron-deficient graphitic carbon environment. This alters the electron density and energy level of the e_g-orbital of the Fe ion, leading to a drastic anodic shift in its redox potential. The electronic and structural features of pyrolyzed Fe–N_4 moieties significantly differ from those of the original macrocycles starting at around 500 °C, as suggested by the disappearance of the FT-EXAFS peaks between 2 and 3 Å that arise from the scattering due to the carbon atoms in the second coordination shell around Fe in the porphyrin or phthalocyanine (Fig. 5b). The additional broad FT-EXAFS peak seen between 2 and 3 Å in the spectrum of FeTPP-600-C shown in Fig. 5b arises from the Fe–Fe scattering in Fe crystalline species (such as metallic Fe, Fe oxides, Fe carbides, Fe nitrides). Such species typically form in parallel with FeN_4 moieties at high temperature, complicating the analysis of FeN_4 moieties formed at temperature > 600 °C. For the present synthesis approach, the majority of these iron crystalline species could however be dissolved with an acid leaching step, performed after pyrolysis. The efficient removal of such species is demonstrated by the absence of FT-EXAFS signal within 2–2.5 Å for FeTPP-800-C for which an acid leaching was performed after pyrolysis (Fig. 5b). The

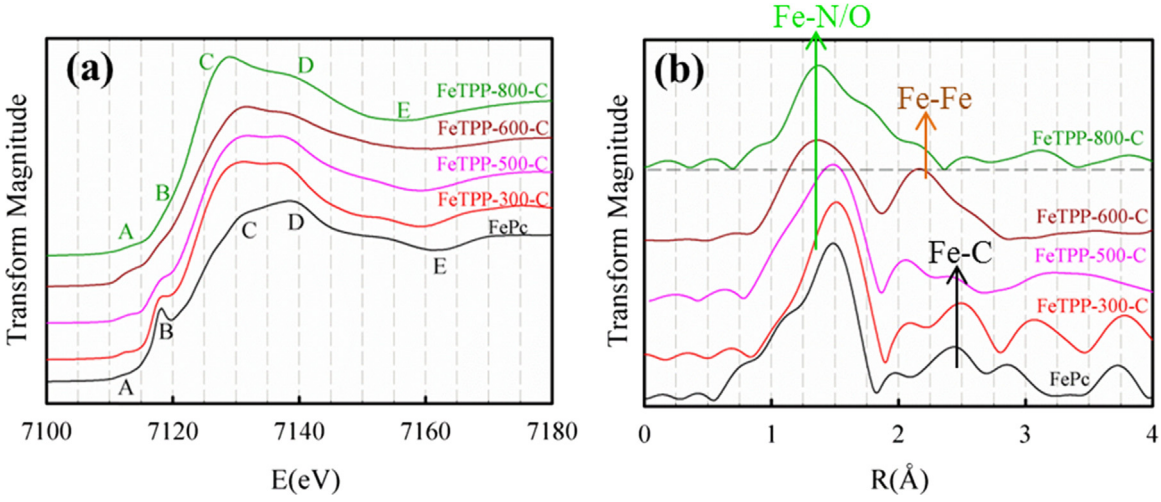

Fig. 5. (a) In situ XANES spectra of FeTPP-pyrolyzed catalysts and of a reference Fe(II) phthalocyanine (bulk $Fe^{2+}Pc$). Spectra were collected at 0.1 V in N_2-saturated 0.1 M KOH to ensure the Fe oxidation state in the Fe–N_4 moieties is +2 for all studied catalysts. FeTPP-800-C was subjected to acid wash before the XANES–EXAFS measurements to remove crystalline Fe species. The ex situ XANES of bulk $Fe^{2+}Pc$ as a square-planar Fe^{2+}–N_4 standard is included. (B) Corresponding in situ EXAFS spectra. Reproduced with permission from Ref. [21]. Copyright 2015, American Chemical Society.

absence of signal within 2–3 Å in the in situ FT-EXAFS spectrum of FeTPP-800-C further suggests that the FeN_4 moieties formed at high temperature are embedded in a disordered carbon support, Otherwise, secondary FT-EXAFS peaks between 2 and 3 Å would be observed as expected from the constructive interference of the scattered waves within ordered structures, just as is the case for FePc or FeTPP-300-C (Fig. 5b). These structural changes observed with EXAFS around 600 °C coincide with the abrupt increase of the fwhm C 1s spectra at 600 °C [22]. Thus, both EXAFS and XPS methods highlight a drastic change of the carbon environment surrounding the Fe–N_x species and that is induced by heat treatment.

Changes in the structural and electronic properties of the central Fe ion upon relocation of the well-defined FeN_4 moiety from a single macrocycle adsorbed on carbon support to a FeN_xC_y moiety integrated into a disordered carbon matrix are directly reflected by the characteristic features (labeled as A–E) of the in situ XANES spectra of the FeTPP-pyrolyzed catalysts (Fig. 5a), which exhibit monotonic trends in amplitude and/or position with increasing pyrolysis temperature. These trends could be well reproduced in theoretical XANES spectra obtained by ab initio FEFF9 calculations by moving the central Fe atom away from the N_4-plane, and fully accounted for by the distortion of the D_{4h} symmetry and the increase in the distance between Fe and N, R_{Fe-N}, as a consequence of the Fe displacement, as demonstrated in our previous work [21].

It is concluded from these results that the new active sites formed upon pyrolysis of macrocycles are distorted Fe-N_4 moieties embedded in the defective pockets and/or the edge-plane sites in disordered carbon supports which provide a π-electron-deficient environment. The observed trends in the ORR activity, $Fe^{2+/3+}$ redox transition potential, and local structures within the FeTPP-pyrolyzed catalysts can be reasonably accounted for by the increasing content of the newly formed active sites with increasing pyrolysis temperature against the decreasing content of the pre-existing square-planar Fe–N_4 species. The possible co-existence of the two sites but with different relative contents in samples pyrolyzed at different temperatures could partially account for the more spread-out experimental Θ_{OH} trends of FeTPP-300-C and FeTPP-800-C compared to the theoretical Θ_{OH} trends (Fig. 4).

These results and their interpretation are also generally consistent with the structural analysis resulting from ex situ Mössbauer spectroscopy of Fe-macrocycle-pyrolyzed catalysts. This spectroscopic method reveals the ubiquitous presence of at least two types of Fe–N_4 moieties in pyrolyzed samples, and also the presence of crystalline Fe species in various proportions depending on the pyrolysis temperature [13,23,24,31,65]. The two types of Fe–N_4 moieties are generally assigned to a Fe–N_4 moiety in medium-spin state (MS) (characterized by a large doublet with large quadrupole splitting, as in bulk FePc, and labeled D2), and to a Fe–N_4 moiety in low-spin state (LS) (characterized by a doublet with smaller quadrupole splitting, labeled D1) [24,53,65,76]. By comparison with ex situ Mössbauer spectra recorded for bulk FePc (where the Fe ion from a single FePc interacts also with N atoms from other FePc molecules stacked in parallel above and below the FeN_4 planes, D2-type signal) and for well-dispersed FePc adsorbed on a carbon support (resulting in the interaction of FePc with the carbon support, D1-type signal, the carbon support with its delocalized electrons acting as an axial ligand), D1 and D2 signals in pyrolyzed catalysts may be empirically assigned to FeN_4 moieties with Fe having out-of-plane and in-plane geometries, respectively. The out-of-plane coordination geometry for D1, measured ex situ with Mössbauer spectroscopy, may however change to in-plane coordination leading to changes in its Mössbauer signal if it were measured in situ at low potential with Mössbauer spectroscopy. The removal of the axial OH adsorbate at $E < E_{redox}$, leading to distinct changes in XANES spectra with electrochemical potential, can be expected to also lead to significant changes for in situ Mössbauer spectra. Until such experiments are carried out, comparison between ex situ Mössbauer and in situ XAS results is difficult to carry out. Mössbauer spectroscopy however clearly reveals the simultaneous presence of two type of FeN_xC_y moieties, the ex situ measurements performed in air likely corresponding to an electrochemical potential close to the open circuit potential in an O_2-saturated liquid electrolyte (as observed for XANES ex situ in air, XANES in situ at OCP).

2.2. Polymer-derived Fe–N–C catalysts

The analogous analysis was also conducted on the in-house PVAG-Fe [30] and the PANI-Fe-C [3] catalysts, as representative polymer-based Fe–N–C catalysts to identify the nature of the active sites, and to verify whether the redox mechanism established on Fe-macrocycle-pyrolyzed catalysts also applies to this sub-group of Fe–N–C catalysts.

As clearly shown in Fig. 6, both polymer-based catalysts exhibit the similar XAS trends as those observed on Fe-macrocycle-pyrolyzed catalysts. That is, XANES shifts toward higher energy with increasing potentials, accompanied by the increased intensity of the FT-EXAFS peak. This clearly indicates that the $Fe^{2+/3+}$ redox kinetics (Eq. (4)) observed on Fe-macrocycle-pyrolyzed catalysts is applicable to polymer-based catalysts. The validity of the redox mechanism is directly supported by the strong correlation between the redox potential of the PVAG–Fe catalyst and the ORR onset potential (Fig. 7). To unambiguously demonstrate the direct involvement of the FeN_xC_y active sites with the $Fe^{2+/3+}$ redox transition in the ORR, the PVAG–Fe catalysts was subjected to the cyanide poisoning test as the cyanide anions efficiently poison the $Fe-N$ centers in non-pyrolyzed and pyrolyzed Fe–N–C materials in both acidic and alkaline electrolytes [30,34]. As seen in Fig. 7, the addition of 10 mM CN^- significantly poisons the Fe–N centers as evidenced by the suppressed redox peaks, leading to a drastic negative shift of the ORR polarization curve. On the contrary, the ORR performance of the Fe–N–C materials free of FeN_xC_y species (e.g., dominated by Fe@N_xC_y species) is not affected by cyanide poisoning test [36]. Therefore, cyanide poisoning test is a valid method to distinguish between FeN_xC_y and Fe@N_xC_y species.

It is noted that the Δμ–XANES of these two polymer-based catalysts are essentially the same as that measured for FeTPP-800-C, and the XANES and FT-EXAFS spectra are also very close (Fig. 8). These XAS results strongly suggest that these two sub-groups of Fe–N–C catalysts share the same type of active site (D1). The same conclusion were drawn based on Mössbauer results that the D1 site was identified in both macrocycle-based catalysts as well as catalysts synthesized using individual Fe, N and C precursors [23,25], including PANI-Fe-C [58].

One trivial but intriguing difference in the final products between the macrocycle-pyrolyzed catalysts and polymer-based catalysts after pyrolysis is suggested by XAS. The XANES and the first derivate of PAVG–Fe and PANI-Fe-C does not show any shoulder at 7117 eV, indicative of the absence of the perfect square-planar Fe–N_4 sites; whereas a clear shoulder is clearly seen in the first derivative of XANES of FeTPP-800-C (Fig. 8), indicating the retaining of the pre-existing square-planar Fe–N_4 sites [21]. This is further supported by the fact that PANI-Fe-C shows a more distorted Fe–N_4 structure compared to FeTPP-800-C, just like FeTPP-800-C with higher D1 content exhibiting a more distorted Fe–N_4 structure compared to FeTPP-300-C (Fig. 9). In addition, whereas spread-out Θ_{OH} trends of FeTPP-300-C and FeTPP-800-C due to the co-existence of multiple sites, both polymer-based catalysts exhibit rather sharp Θ_{OH} trends as increasing around 0.75 V, corresponding to the $Fe^{2+/3+}$ redox potential of the D1 site

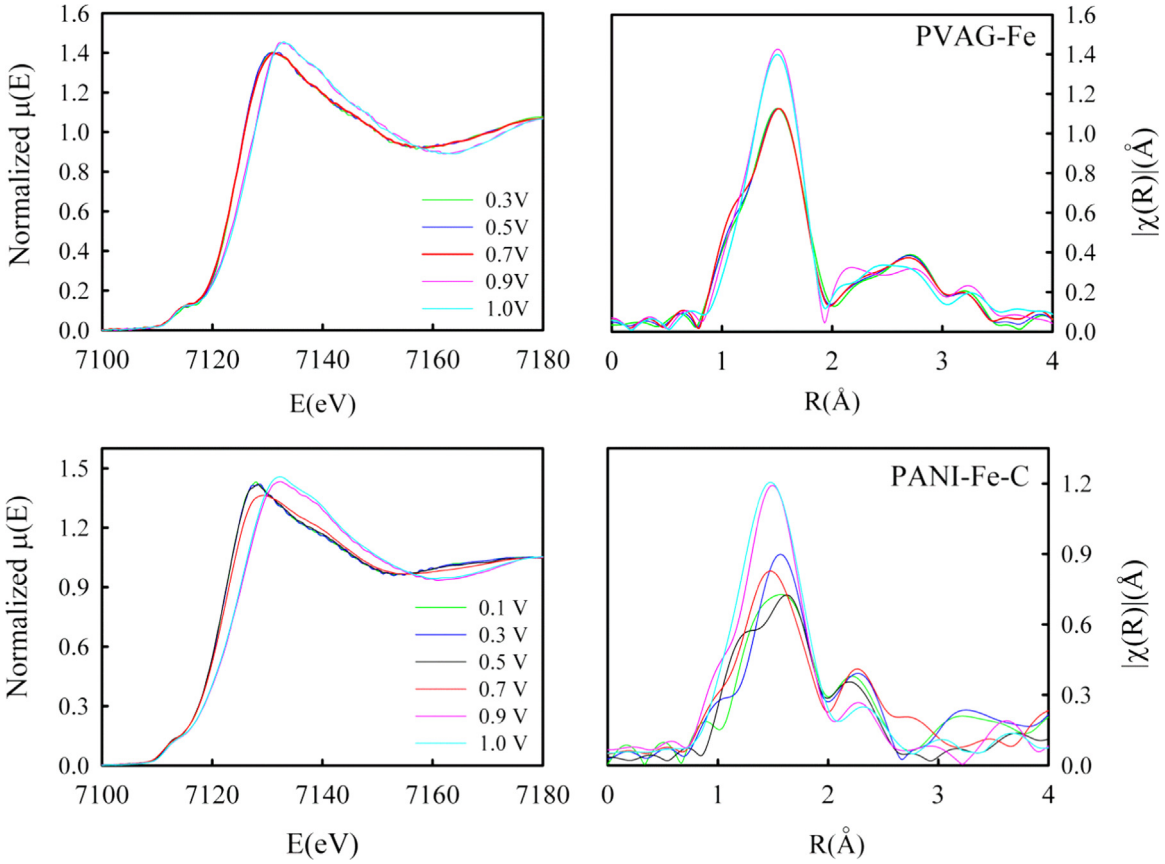

Fig. 6. (left) Potential dependent normalized Fe K-edge XANES spectra collected in N_2-saturated 0.1 M $HClO_4$; (right) Fourier Transform of the extended region of the XAS spectra collected in situ at the Fe K-edge (7112 eV) of the PVAG-Fe (top) and PANI-Fe-C catalyst (bottom).

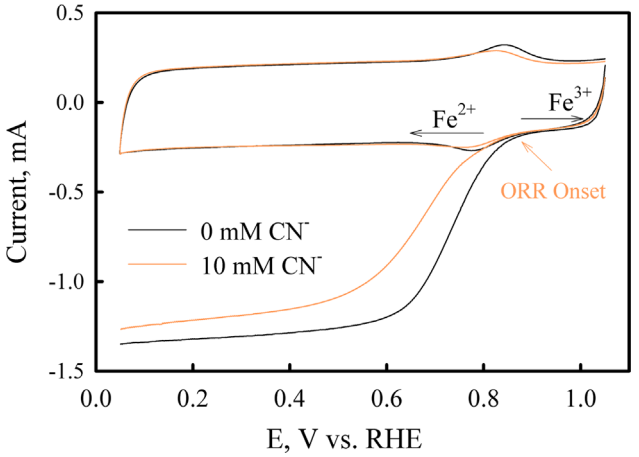

Fig. 7. CV of the PVAG-Fe catalyst obtained in CN^--free (black) and 10 mM CN^- (orange) 0.1 M $HClO_4$ electrolyte with the clear $Fe^{2+/3+}$ redox transition between 0.7 and 0.9 V and the corresponding ORR polarization curves collected at 1600 rpm. Scan rate: 20 mV/s; loading: 0.6 mg/cm^2 on 5.61 mm glassy carbon disk electrode. Reproduced with permission from Ref. [30]. Copyright 2014, American Chemical Society.

(Fig. 10). In addition, this $Fe^{2+/3+}$ redox transition peak is also observed by the square wave voltammetry method, the square-planar Fe–N_4 associated $Fe^{2+/3+}$ redox transition peak around 0.15 V observed on FeTPP-300-C is absent. The lack of the perfect square-planar Fe–N_4 sites in these two polymer-based catalysts may be attributed to its different carbon environment from that of macrocycle-based catalysts owing to the different precursors.

Another difference between the polymer-based and macrocycle-based catalysts is that the crystalline Fe species in the polymer-based catalysts is more stable in acidic environment than that in the macrocycle-based catalysts as evidenced by the Fe–Fe scattering peak around 2.0 Å, which is ascribed to the protection by the surrounding onion-like graphitic carbon nanoshells as observed by high-resolution transmission electron microscopy (HRTEM) [3]; whereas the crystalline Fe species in FeTPP-pyrolyzed catalysts are mostly unprotected and are spontaneously dissolved in acid. It was proposed that the metallic iron encapsulated in carbon nanotubes [36] or graphitic layers [14,35] may be a new active site for ORR, but the active role of this site is under extensive debate currently, as aforementioned. Therefore, in order to obtain a clear structure/activity correlation of Fe–N–C catalysts, it is necessary to gain better control over the final products upon heat temperature treatment, leading to the preferential formation of FeN_xC_y moieties. As shown below, this can be readily acquired by utilizing the SSM method (Fig. 11).

2.3. Sacrificial support method (SSM)-based catalysts

Both Fe-CTS and Fe-AAPyr catalysts were prepared using the Sacrificial Support Method (SSM) [28,77–80] with details given in the supporting materials. The Iron speciation in the representative Fe-CTS and Fe-AAPyr catalysts is characterized with ^{57}Fe Mössbauer spectroscopy together with in situ X-ray absorption spectroscopy (XAS) (Fig. 11). Two FeN_xC_y moieties (D1 and D2) are identified in both Fe-AAPyr and Fe-CTS catalysts resulting in two doublets (Fig. 11a and Table 1), which are assigned as a four-fold nitrogen coordination of Fe^{2+} in low-spin (LS) and medium-spin state (MS), respectively [23,25]. Consistently, the single FT-EXAFS peak around 1.6 Å (without phase-correction) is assigned to the

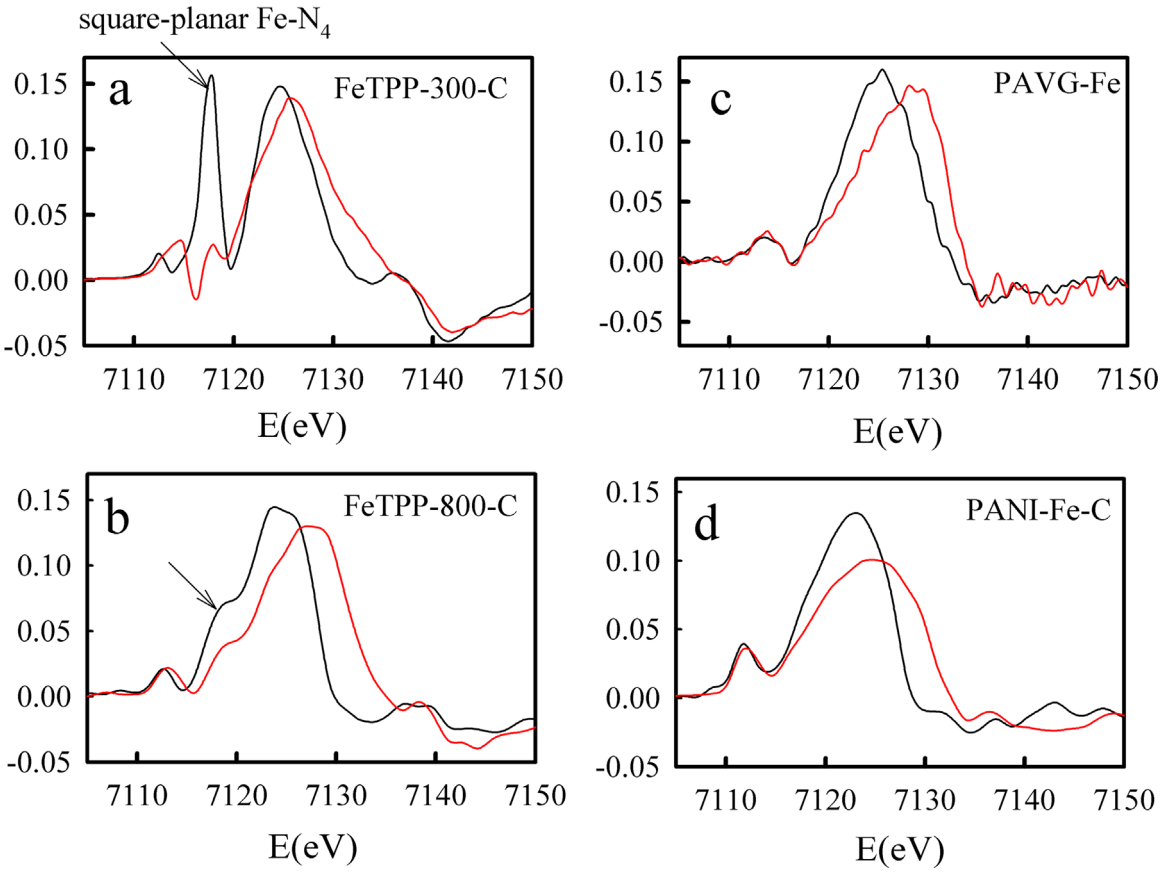

Fig. 8. First derivative XANES at the Fe K-edge of (a) FeTPP-300-C, (b) FeTPP-800-C, (c) PAVG-Fe, and (d) PANI-Fe-C at 0.1 V (black) and 1.0 V (red), respectively.

Fe–N signal from Fe–N_4 moieties based on EXAFS fitting results (Table 2). The D1 and D2 exact structure is subject of ongoing research related to the exact site structure and to the integration of FeN_4 moieties, which can be viewed either at defect sites within a graphene layer, or as a structure bridging two graphene zigzag-or-armchair-edges [13,22,23]. Interestingly, the Mössbauer parameters and relative contents of D1 and D2 are almost identical to those for a MOF derived catalyst labeled Fe-0.5-dry in Zitolo et al.'s recent work [13], resulting in superimposed overall spectra for two catalysts prepared from completely different precursors. This supports the universality of the structures corresponding to D1 and D2 in pyrolyzed FeN_xC_y materials. In addition to the two doublets (D1 and D2), three more Fe species were identified in the Fe-CTS catalyst resulting in a singlet, and two sextets (Fig. 11c), but were absent in the Fe-AAPyr catalyst. The singlet is assigned to either γ-Fe or super paramagnetic Fe nanoparticles, [23] while the sextet's parameters match those of α-Fe and iron carbide [23,25].

The different distribution in nitrogen species is also confirmed by XPS (Fig. 12). Fe-AAPyr shows much larger relative amounts of metal coordinated to iron Fe–N_4 (399.5 eV) and pyridinic nitrogen

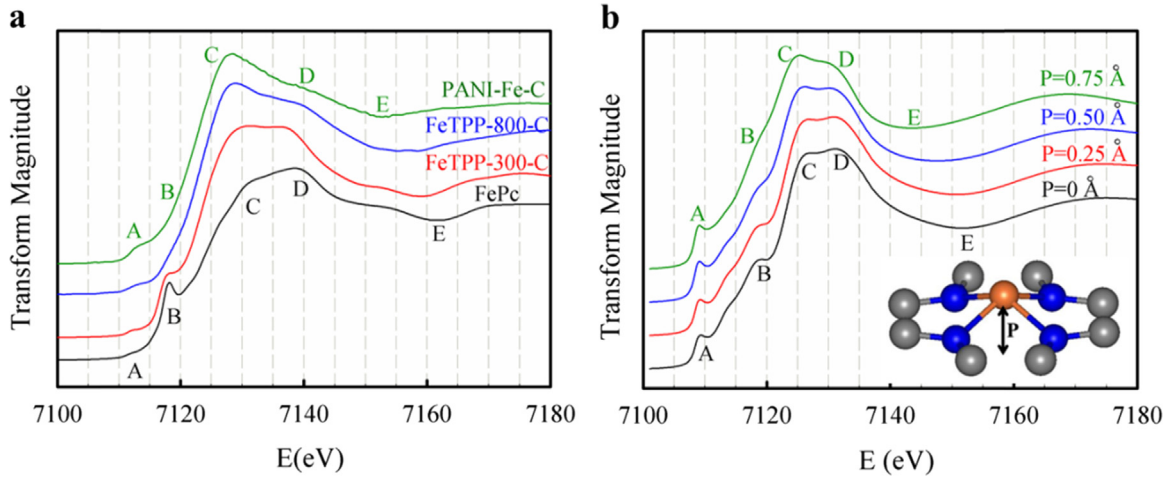

Fig. 9. (a) Catalyst XANES spectra collected at 0.1 V in N_2-saturated 0.1 M $HClO_4$; the XANES of bulk FePc as a square-planar Fe^{2+}–N_4 standard is included. b) XANES spectra calculated by FEFF9 based on the Fe–N_4–C_8 model (inset) with various central Fe displacements (denoted as P). Note the change of the relative intensity of features C and D. Reproduced with permission from Ref. [21]. Copyright 2015, American Chemical Society.

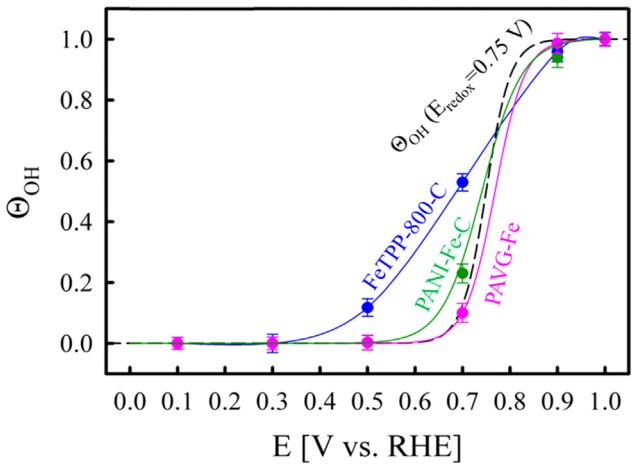

Fig. 10. Experimental Θ_{OH}(s) as a function of potential for FeTPP-800-C, PANI-Fe-C, and PAVG-Fe catalysts, in comparison to the calculated Θ_{OH}(s) derived from Eq. (2) using the redox potential of 0.75 V and the temperature of 298 K.

Table 1
Mössbauer fitted parameters for the Fe-AAPyr and Fe-CTS catalyst.

Component (assignment)	IS (mm s^{-1})	QS (mm s^{-1})	H (T)	LW (mm s^{-1})	Relative absorption area (%)
Fe-CTS					
Param. or γ-Fe	−0.07	–	–	0.67	14
D1 ($Fe^{II}N_4$ LS)	0.33	0.98	–	0.80	30
D2 ($Fe^{II}N_4$ MS)	0.51	2.34	–	1.83	44
Fe_xC	0.29	–	20.2	0.62	10
α-Fe	0.04	–	33.5	0.37	4
Fe-AAPyr					
D1 ($Fe^{II}N_4$ LS)	0.38	1.20	–	0.90	67
D2 ($Fe^{II}N_4$ MS)	0.62	2.71	–	1.24	33

(398.5 eV). As was reported before, the pyridinic nitrogen peak has also contribution from disordered metal centers such as Fe–N_3, Fe–N_2, and Fe–N [32].

The different content in the final products between these two catalysts revealed by ex situ Mössbauer spectroscopy and XPS is further confirmed by in situ XAS. The two FT peaks displayed in Fig. 11d clearly confirm the plurality of chemistries in the Fe-CTS catalyst. The second FT peak at ~2.1 Å (all the radial distances given in this work are without phase correction) can be well fitted as a Fe–Fe shell with a bond length of ~2.51 Å. This bond length is close to the Fe–Fe bond length in iron carbide or iron nanoparticles (2.48 Å), confirming that the Fe-CTS catalyst contains some inorganic iron species that are stable under the acidic and oxidizing environment. The small N_{Fe-Fe} (~1.2) coordination number suggests either the iron carbide content is low compared to that of the Fe–N_x species, and/or the particle size is small. This is consistent with the small amounts of γ-Fe and Fe_xC obtained by Mössbauer and absence of visible nanoparticles in high resolution TEM [19]. The constant peak intensity with the operating potential indicates the iron carbide is not directly involved in the reaction, thereby excluding the dual-site mechanism with the exposed inorganic Fe species as the second site [30,37].

The first FT peak at ~1.6 Å arises from the Fe–N/Fe–C/Fe–O (nitrogen, carbon, and oxygen cannot be distinguished as surrounding atoms by XAS) scattering. Owing to the bulk average

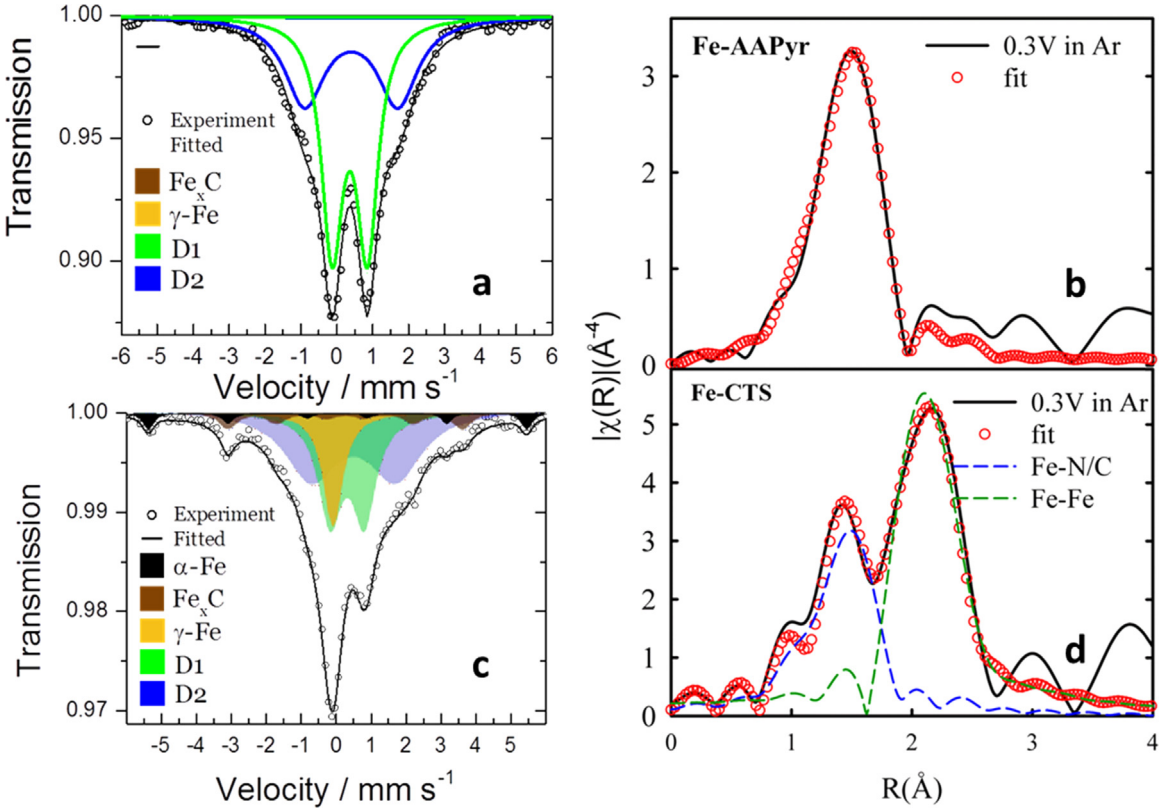

Fig. 11. Mössbauer absorption spectrum and its deconvolution for the Fe-AAPyr (a) and its FT-EXAFS spectra (b) and Mössbauer absorption spectrum for the Fe-CTS catalysts (c) and the corresponding FT-EXAFS spectra (d) [spectra Fig. 11c and d are reproduced from an earlier work [19]; copyright 2015, Elsevier]. The measurement was performed at room temperature and calibrated vs. α-Fe foil. Fourier Transforms of the Fe K-edge XAS data and the corresponding EXAFS fits.

Table 2
Results of fitting EXAFS data obtained under in situ electrochemical operating conditions for the Fe-CTS and Fe-AAPyr catalysts synthesized at 900 °C and second heat treatment in NH_3 at 950 °C. The measurements were performed at 0.3 and 0.9 V vs. RHE in the N_2-saturated 0.1 M $HClO_4$ electrolyte at room temperature. Coordination number (N), phase-corrected bond length (R), Debye–Waller factor (σ^2), and edge shifts (E_0) are shown for each interaction. The results of Fe-CTS are obtained from Ref [19]; copyright 2015 Elsevier.

	Fe–C/N/O path				Fe–Fe path			
Fe-CTS								
Potential	N	R (Å)	σ^2 (Å^2) $\times 10^{-3}$	E_0 (eV)	N	R (Å)	σ^2 (Å^2) $\times 10^{-3}$	E_0 (eV)
0.3 V	3.6(7)	2.02(2)	9(3)	−5(1)	1.2(3)	2.51(1)	9(3)	−5(1)
0.9 V	4.0(8)	2.01(2)	4(2)	−6(2)	1.3(3)	2.52(1)	4(2)	−6(2)
Fe-AAPyr								
Potential	N	R (Å)	σ^2 (Å^2) $\times 10^{-3}$	E_0 (eV)	N	R (Å)	σ^2 (Å^2) $\times 10^{-3}$	E_0 (eV)
0.3 V	4.3(6)	2.05(2)	7(3)	−3(1)	–	–	–	–
0.9 V	5.2(8)	2.03(2)	5(2)	−2(2)	–	–	–	–

S_0^2 fixed at 0.88 as obtained by fitting the iron reference foil. The Fourier-transformed (FT) EXAFS data were fitted under simultaneous $k^{1,2,3}$ weighting, R range 1.0–3.0 Å, k range 1.95–10.96 Å^{-1}. The statistical errors of the least-squares fits were determined by ARTEMIS.

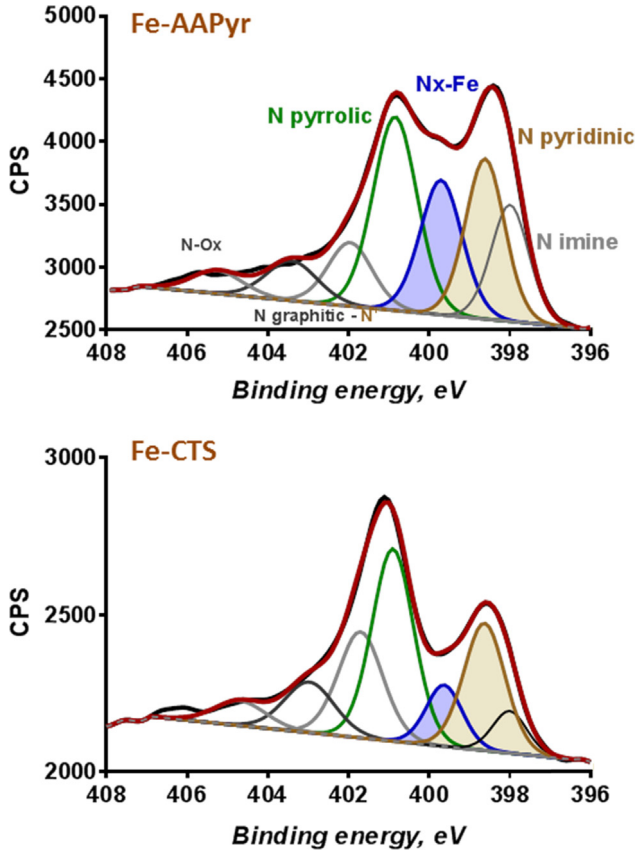

Fig. 12. XPS high resolution N 1s spectra and its deconvolution for the Fe-AAPyr and Fe-CTS catalysts. Peaks highlighted are due to Fe–N_4 (399.5 eV) and pyridinic N (398.5 eV).

nature of EXAFS technique, the corresponding coordination number at 0.3 V (3.6) is a weighted average of the coordination number of the Fe–N bonds in the Fe–N_x species and the Fe–C bonds in the iron carbide. As the iron carbide content is relatively low, and the first shell Fe–C coordination number is small (≤ 3), it is reasonable to infer that the Fe–N coordination number in the Fe–N_x species is 4. The increase in the coordination number as the potential is increased to 0.9 V, which has been observed on macrocycled-pyrolyzed and polymer-based catalysts shown above, suggests the adsorption of oxygenated species onto the Fe–N_4 sites (Eq. (4)). These hypotheses are further supported by the Δμ analysis shown below (Fig. 13). In contrast to Fe-CTS, Fe-AAPyr contains only one FT peak located around 1.6 Å, and the corresponding EXAFS fitting result of N coordination number is around 4. This confirms that Fe-AAPyr is dominated by Fe–N_4 moieties. The lack of the second FT peak verifies that Fe-AAPyr does not contain metallic Fe species under in situ operando conditions.

The XANES of the Fe-CTS and Fe-AAPyr catalysts at various potentials are displayed in Fig. 13. The absence of the peak at ~7117 eV, which is the fingerprint of the square-planar Fe–N_4 moiety, [22,75,81] is indicative of the lack of the intact square-planar Fe–N_4 moiety in these catalysts. The XANES edge shifts to higher energy as the potential is increased from 0.3 to 0.9 V, indicating the increase of the Fe oxidation state. The corresponding Δμ signal (Fig. 13, right) is essentially identical to that obtained on FeTPP-800-C (Fig. 3) and polymer-based catalysts (Fig. 8), and can be nicely mimicked by the theoretical Δμ spectrum obtained using the FeN_4C_y cluster models with either a partial ($y=10$) or complete destruction ($y=8$) of the carbon methane bridges [22]. While the O adsorption onto the Fe center can be confirmed by the surface sensitive Δμ–XANES analysis, the O and OH adsorbate cannot be distinguished by this technique because they give the similar Δμ–XANES signals. Similarly, the end-on and side-on adsorption of O_2 molecules on the FeN_xC_y site, which were proposed by Zitolo et al. [13] based on ex situ XAS, cannot be distinguished by Δμ–XANES analysis as well.

In addition to its high ORR activity, the Fe-CTS catalyst exhibit decent durability in both RDE and fuel cells upon multiple testing protocols [19]. It has been demonstrated that the FeN_x sites are stable up to 1.0 V, but the carbon oxidation occurs at high potential (>0.9 V) will destruct the FeN_xC_y active sites [82]. In addition, the Fe leaching from inorganic Fe particles occurring at low potential (<0.7 V) is likely to induce the Fenton-type process that leads to peroxide initiated free-radical formation [30,82]. In addition, Dodelet's group recently attributed the initial rapid degradation of some Fe–N–C catalysts in fuel cells to the micropore flooding that is caused by the oxidation of the carbon support leading to the transformation from hydrophobic catalyst layers into hydrophilic ones [83]. Therefore, the high durability of the Fe-CTS catalyst is likely attributable to the graphitic carbon layers that are more tolerant to carbon corrosion at high potentials, and well protects the wrapped inorganic Fe species from acidic dissolution.

Therefore, the combination of a variety of microscopic and spectroscopic techniques confirms that the content of inorganic iron species in the final products synthesized via SSM method is controllable, from relatively large content down to their complete absence. More importantly, the combination of in situ EXAFS, XANES, and Δμ results strongly suggests that the catalytically active sites (Fe–N_4) in all the studied catalysts, irrespective of the precursors materials (macrocycles or individual Fe, N, and C precursors), the synthesis method (wet chemical impregnation or SSM), and final ORR-active Fe-species (with or without

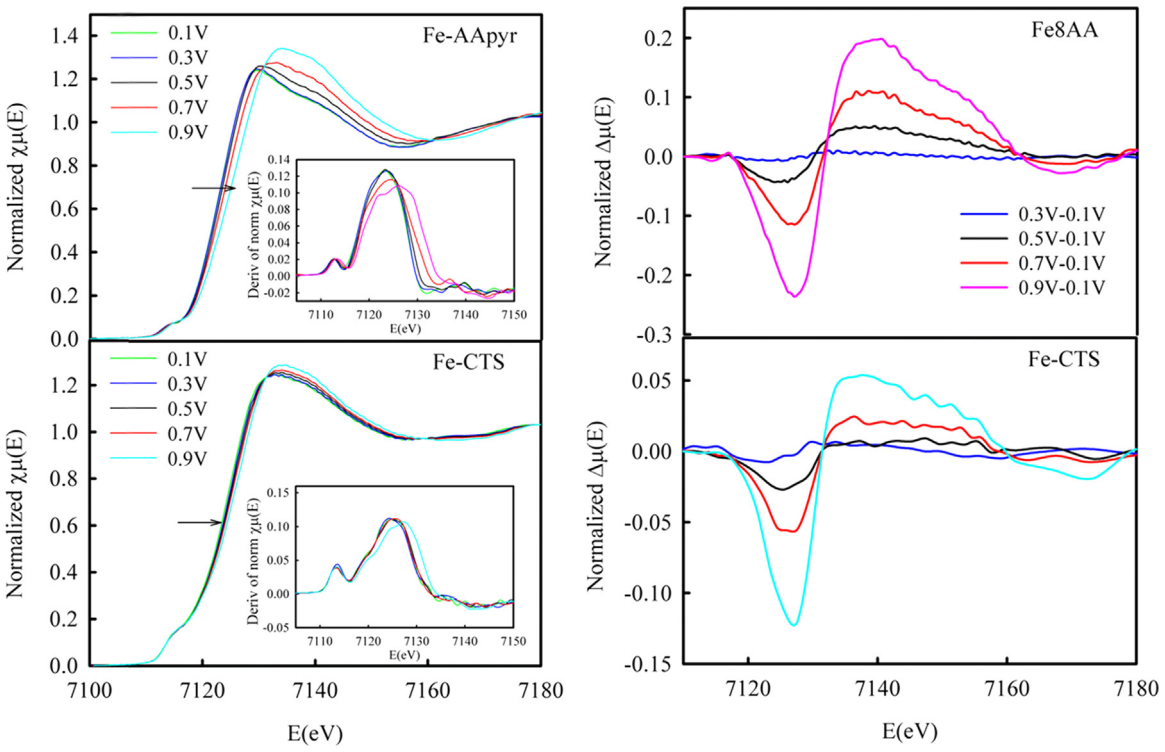

Fig. 13. XANES (left) at the Fe K-edge with concomitant first derivatives (insets) and derivative Δμ–XANES spectra (right).

concomitant presence of inorganic iron species), are formed via the covalent incorporation of distorted Fe–N_4 moieties in the divacant defective centers on the carbon basal plane or in armchair edges of two adjacent graphene layers. In addition, the Fe^{2+}–N_4 active site at 0.3 V undergoes redox transition to a pentacoordinate $(H)O-Fe^{3+}-N_4$ at 0.90 V, and the adsorption of the *OH trigged by the Fe^{2+}/Fe^{3+} redox transition poisons the active sites (Eq. (4)), thereby providing experimental evidence of the redox mechanism.

Compiling the results obtained on a variety of Fe–N–C materials shown above, the D1 site is commonly found in all the pyrolyzed Fe–N–C catalysts irrespective of the precursor materials and synthesis routes. It is widely believed that this site is responsible for the decent ORR activities of pyrolyzed Fe–N–C catalysts measured in acid [23,24,53]. Based on this assumption, the intrinsic activity of D1 in terms of turnover frequency (TOF) has been estimated by different research groups to understand the high catalytic activity obtained with low Fe loadings. The value obtained at the potential of 0.8 V vs. RHE (the potential set by DOE for non-PGM catalyst activity evaluation) varies drastically from 0.02 to 0.93 e s^{-1} $sites^{-1}$ depending on the Fe loadings and the methods employed to estimate the availability of the active sites [25,38,84,85]. It is noted that the activity of D1 may change significantly upon the basicity of the carbon support, and hence the derived TOF does not exclusively reflect the structure-related activity of the site. Although a rigorous method is yet to be developed to determine the TOF of D1 accurately, these studies strongly support the high average intrinsic activity of the D1 site in pyrolyzed Fe–N–C catalysts.

2.4. MOF-based catalysts

The development of MOF-based materials as ORR catalysts was pioneered by Dodelet's [20] and Liu's [86] groups. Since then, MOF-based catalysts caught increased attention owing to their high activity and stability, which is attributable to the favorable carbon morphology obtained from the sacrificial pyrolysis of highly porous MOFs. These carbon structures can host a high density of active sites, and are also very open structures facilitating the mass transport of ORR-related species towards and away from the active sites [14,20]. Recently, a robust MOF-based catalyst with exceptional ORR activity in both RDE and PEMFC was developed by Jaouen's group [13]. For all these previously reported MOF-based catalysts, the FeN_xC_y moieties were shown to be the active sites. In contrast, the nature of active sites in the FePhen@MOF-$ArNH_3$ catalyst reported by us previously [14] is fundamentally different. This material is devoid of FeN_xC_y moieties, as demonstrated by combined ^{57}Fe Mössbauer spectroscopy and in situ X-ray absorption spectroscopy (XAS) (Fig. 14), yet shows very high ORR activity [14]. Specifically, the D1 and D2 doublets characteristic for FeN_xC_y moieties, ubiquitous in all other Fe–N–C catalysts hitherto studied with Mössbauer spectroscopy, are not seen in the Mössbauer spectrum of FePhen@MOF-$ArNH_3$ (Fig. 14, top). In addition, the Fe K edge FT of the EXAFS for FePhen@MOF-$ArNH_3$ does not contain the characteristic Fe–N/O peak at 1.6 Å (indicative of Fe–N/C/O interaction) and is characterized instead by a peak at ~2.2 Å coinciding with Fe–Fe scattering in metallic Fe and Fe_3C (Fig. 14, bottom). The EXAFS fitting also suggests that the catalyst is dominated by inorganic iron species with only minimal amount of Fe–N–C species (if there is any). In addition, the Fe K edge XANES energy of FePhen@MOF-$ArNH_3$ remains unchanged with increasing electrochemical potential, further excluding the presence of FeN_xC_y sites that would otherwise exhibit the $Fe^{2+/3+}$ redox transition within the potential window as shown above. These results lead us to conclude that FePhen@MOF-$ArNH_3$ is dominated by Fe/Fe_3C nanoparticles encapsulated by nitrogen-doped carbon shells (Fe/Fe_3C@N-C) and there are no detectable Fe–N_x moieties present under ex situ and in-situ conditions. Therefore, the redox mechanism established on FeN_xC_y sites does not apply for the FePhen@MOF-$ArNH_3$ catalyst. Interestingly, these comparative studies show that the FeN_xC_y and Fe@N_xC_y sites can be distinguished by in situ XAS: the former display a clear $Fe^{2+/3+}$ redox behavior leading to a positive shift of the Fe XANES spectra;

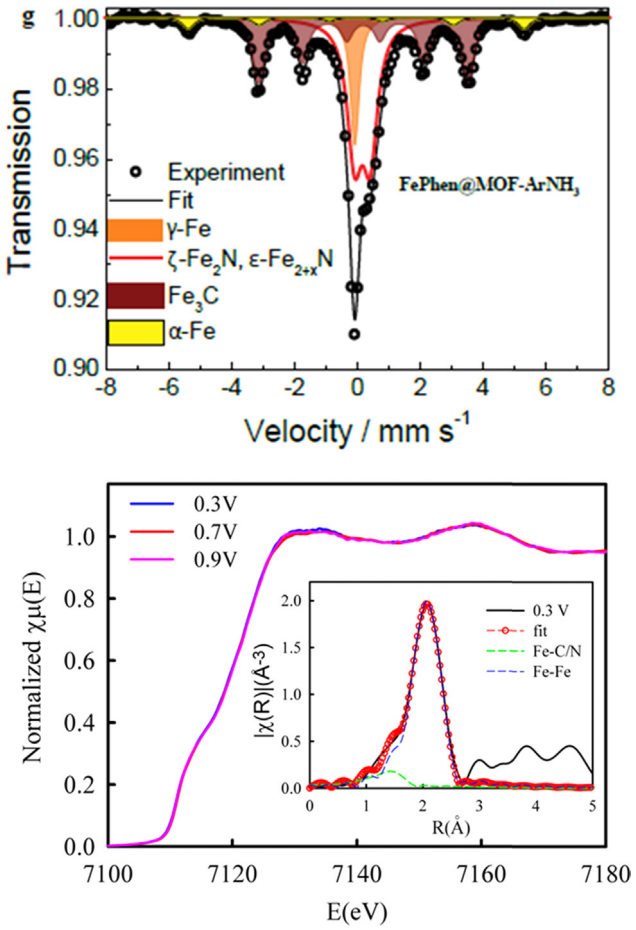

Fig. 14. Mössbauer absorption spectrum and its deconvolution for the FePhen@MOF-ArNH$_3$ catalysts (top); Reprinted with permission from Macmillan Publishers Ltd. [Nature Communication] Ref. [14]. Copyright (2015) (top); XANES and FT-EXAFS of the Fe K-edge XAS data with the EXAFS fits (bottom).

whereas there is no shift for the latter case for which the Fe is not directly involved into the ORR.

To understand the causes of the different final products between the FePhen@MOF-ArNH$_3$ catalyst and the catalysts synthesized via SSM method, pore size distributions calculated from mercury intrusion porosimetry are shown in Fig. 15, with calculated pore modes given in the accompanying table. Both catalysts exhibited significant pore volume in the 100–300 nm range. However, whereas the SSM materials demonstrate a significant pore mode at nanometer length scales, no such mode is observed in the MOF catalyst. The presence of micropores (pore size <2 nm) has been shown to be positively correlated to the ORR activity and density of FeN$_x$C$_y$ moieties for Fe–N–C catalysts whose activity is based on FeN$_4$ moieties [13,39,48]. The absence of micropores, absence of FeN$_x$C$_y$ moieties and yet high ORR activity of FePhen@MOF-ArNH$_3$ are consistent with the conclusion that the active sites of this specific material are fundamentally different. In addition, the disordered carbon morphology in the MOF-based catalyst [14] is also different from the graphitized carbon morphology in the SSM-synthesized materials [19]. It is likely that the Fe–N$_x$ sites containing only one single Fe atom are preferentially located in small pores, while the agglomerated Fe nanoparticles are better hosted and protected by graphitized carbon with relatively large pores. Although the mechanisms governing the types and relative content of various Fe-containing species in the final products after high temperature pyrolysis are unclear, we do have some controls over the final products: non-PGM catalysts with only Fe–N–C moieties, or only Fe@N-C, or both can be readily produced.

It is noted that the activity of the FePhen@MOF-ArNH$_3$ catalyst is comparable to those state-of-the-art Fe–N–C catalysts, [14] and much higher than the structurally similar materials previously reported [35,36,39]. For this group of catalyst, it is believed that the catalytic activity arises from the electron transfer from Fe particles to the N-doped carbon leading to a decreased local work function on the carbon surface, thereby drastically increasing the catalytic activity of the carbon [36]. This is in lines with the recent work by Guo et al. [42] showing that the carbon atoms next to pyridinic N with Lewis basicity (without any metal) are the active sites for ORR under acidic conditions. Moreover, they further showed that the ORR onset potential increases up to 0.91 V with increasing nitrogen content, approaching those (0.95 ± 0.02 V) of state-of-the-art Fe–N–C catalysts [3,88]. Therefore, it is inferred that the buried Fe particles can further boost the catalytic activity of nitrogen-doped carbon, and the high ORR activity of FePhen@MOF-ArNH$_3$ is caused by the high BET area and the high nitrogen content associated with MOFs. Despite the uncertainty of the active site, this type of catalyst is promising as future non-PGM catalysts because its unique morphology brings on the potential of (1) hosting greater active site density; (2) eliminating Fenton-type process involving exposed iron ions in peroxide initiated free-radical formation [14]; and (3) scale up [89].

In addition to the high catalytic activity toward ORR, this type of catalyst (M@N$_x$C$_y$ (M=Fe, Co, and Ni) have been recently shown

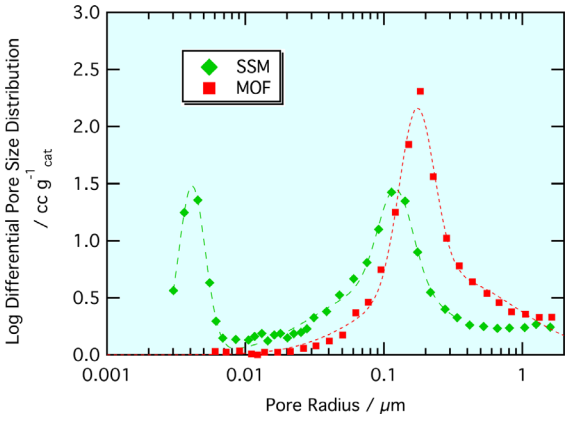

SSM	
r_0 / nm	Vol. Fraction
4.1	0.27
98	0.52
121	0.21
MOF	
r_0 / nm	Vol. Fraction
173	0.36
277	0.64

Fig. 15. Pore size distributions by mercury intrusion porosimetry (MIP) for catalyst layers prepared from SSM and MOF catalyst materials. Dashed lines indicate deconvolution of distributions into three (SSM) and two (MOF) log-normal distributions with mean radius, r_0, and volume fractions indicated in the table. SSM data from Ref. [87].

by various groups to exhibit high catalytic activity and durability toward hydrogen evolution reaction (HER) competitive to commercial Pt/C in acidic electrolytes [90–93]. The high activity was attributed by Bao et al. to the optimization of the electronic structure carbon nanotube toward HER synergistically induced of the transition metal and nitrogen dopants [93]. In the meanwhile, Laasonen et al. [41] attributed to the high HER activity and durability of the Fe@N_xC_y catalyst to the unique single carbon layer that does not prevent desired access of the reactants to the vicinity of the iron nanoparticles but protects the active metallic core from oxidation. Although the nature of active sites and the mechanistic origin of the high HER activity of this type of catalyst are yet clear, these studies demonstrated new opportunities for designing and tuning properties of MOF-derived electrocatalysts for largescale water electrolysis.

2.5. Scale-up of catalysts formulations

The Fe-CTS catalyst was successfully scaled up to 50 g by Pajarito Powder, while the scale of the FePhen@MOF-ArNH_3 catalyst is ongoing with trajectory to similar manufacturing scales demonstrated. Both approaches required several modifications of the processing steps and conditions of the original synthesis approaches.

The approach adopted for the Fe-CTS catalyst involved blends of materials derived using two separate approaches: one of a University of New Mexico group's silica templating methodology, referred to as Fe-CTS, and a UNM-CBDZ approach. The Fe-CTS was derived using the mechano-chemical approach of ball milling an organic charge transfer salt (Nicarbazin) in the presence of Fe salt and the latter using an aqueous formulation of a non-chelating material, carbendazim, with Fe salt, and both were supported on silica followed by several pyrolysis and etching steps. Typical blends comprised of a 1:1 mixture. As a result, this catalyst exhibit a highly porous carbon matrix structure, which not only hosts high active site density, but also provides high mass transport; both are critical for PEMFC performance. Fig. 16 shows the evolution of the blend formulations, Gen 1(CTS only) and Gen 2(CTS & CBDZ), made using variations in precursors and silica templating materials. The final formulation Gen2B scaled to 50+grams/batch shows performance with 70 mA/cm^2 at 0.8 V and 1000 mA/cm^2 at 0.4 V achieved using 3 mg/cm^2 loading gas diffusion electrode in hydrogen/air PEMFCs with 2.5 bar air and 80 °C at 100% humidification. The low current density DOE target of 30 mA/cm^2 at 0.8 V (uncorrected) [89] has been exceeded by current state-of-the-art performance at 70 mA/cm^2 current density. Meanwhile, the higher current density target of 1 A/cm^2 at 0.4 V (infrared (IR)-corrected) [89] has nearly been met with an uncorrected current activity of 0.92 A/cm^2 (uncorrected) and 1.05 A/cm^2 (IR-corrected).

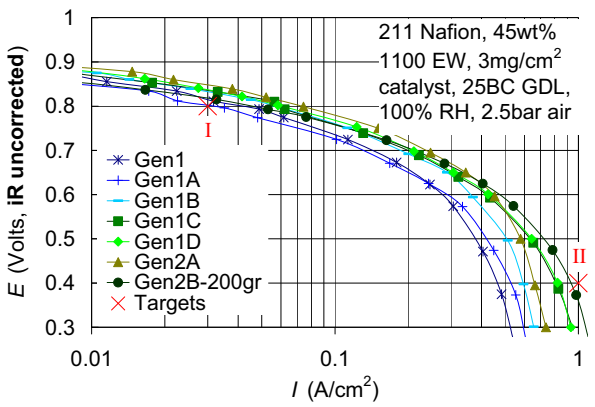

Fig. 16. The H_2/air PEMFC performance of Fe-CTS catalyst scaled to 50 g per batch.

3. Summary and conclusions

Herein, a combination spectroscopic techniques confirms that the high activity observed for most pyrolyzed Fe-based catalysts, irrespective of the precursors materials (macrocycles or individual Fe, N, and C precursors), the synthesis method (wet chemical impregnation or SSM), and final Fe-species (with or without inorganic iron species), can mainly be attributed to a single active site: non-planar Fe–N_4 moiety embedded in distorted carbon matrix characterized by a high potential for the $Fe^{2+/3+}$ redox transition in acidic electrolyte/environment, which is likely formed via the covalent incorporation of distorted Fe–N_4 moieties in the defective centers on the carbon basal plane or in armchair edges of two adjacent graphene layers. This Fe^{2+}–N_4 active site at 0.3 V undergoes redox transition to a penta-coordinate $HO-Fe^{3+}-N_4$ at 0.90 V, and the adsorption of the *OH trigged by the Fe^{2+}/Fe^{3+} redox transition poisons the active sites, thereby providing experimental evidence of the redox mechanism. Moreover, a highly active MOF-based catalyst devoid of any Fe–N moieties was also developed, and the active sites were identified as nitrogen-doped carbon fibers with embedded iron particles that are not directly involved in the oxygen reduction pathway. The high ORR activity and durability of catalysts involving this site in fuel cells are attributed to the high density of active sites and the elimination or reduction of Fenton-type processes. The latter are initiated by hydrogen peroxide but are known to be accelerated by iron ions exposed to the surface, resulting in the formation of damaging free-radicals. We expect that the comprehensive understanding of the synthesis-products correlations, nature of active sites, and the reaction mechanisms acquired here by systematically studying a broad variety of M–N–C materials under in situ conditions will provide guidelines to rational design of this type of non-PGM catalysts.

Acknowledgments

The PANI-derived catalysts were prepared and provided by Gang Wu (Department of Chemical and Biological Engineering, University at Buffalo, The State University of New York, Buffalo, NY) and Piotr Zelenay (Materials Physics and Applications Division, Los Alamos National Laboratory, Los Alamos, NM 87545). We appreciate financial assistance from the U.S. Department of Energy, EERE (DE-EE-0000459). Use of the National Synchrotron Light Source, Brookhaven National Laboratory (BNL), was supported by the U.S. Department of Energy, Office of Basic Energy Sciences. Synchrotron spectroscopy in this publication was made possible by the Center for Synchrotron Biosciences grant, P30-EB-009998, from the National Institute of Biomedical Imaging and Bioengineering (NIBIB). Support from beamline personnel Dr. Erik Farquhar and Mark Chance (X3B) are gratefully acknowledged. Use of the Stanford Synchrotron Radiation Lightsource, SLAC National Accelerator Laboratory, is supported by the U.S. Department of Energy, Office of Science, Office of Basic Energy Sciences under Contract no. DE-AC02-76SF00515. Use of Beamline 2-2 at SSRL was partially supported by the National Synchrotron Light Source II, Brookhaven National Laboratory, under U.S. Department of Energy Contract no. DE-SC0012704. Use of the beamline 9-BM in Advanced Photon Source, an Office of Science User Facility operated for the U.S. Department of Energy (DOE) Office of Science by Argonne National Laboratory, was supported by the U.S. Department of Energy under Contract no. DE-AC02-06CH11357. MRCAT operations are supported by the Department of Energy and the MRCAT member institutions. This research used resources of the Advanced Photon Source, a U.S. Department of Energy (DOE) Office of Science User Facility operated for the DOE Office of Science by Argonne National Laboratory under Contract no. DE-AC02-06CH11357.

This article is dedicated to the memory of Professor David Ramaker from the Department of Chemistry, George Washington University, who passed away on April 12th, 2016. It was his pioneering vision and efforts which led to the development of advanced synchrotron-XANES based Δ-Mu technique as a surface science tool for studying catalysis including electrocatalysis under in situ operando conditions. This article is testament to a long and fullfilling collaboration and legacy of several graduate students' thesis.

Appendix A. Supplementary material

Supplementary data associated with this article can be found in the online version at http://dx.doi.org/10.1016/j.nanoen.2016.03.025.

References

[1] R. Jasinski, Nature 201 (1964) 1212–1213.
[2] E. Yeager, Electrochim. Acta 29 (1984) 1527–1537.
[3] G. Wu, K.L. More, C.M. Johnston, P. Zelenay, Science 332 (2011) 443–447.
[4] M. Lefèvre, E. Proietti, F. Jaouen, J.-P. Dodelet, Science 324 (2009) 71–74.
[5] N. Alonso-Vante, H. Tributsch, O. Solorza-Feria, Electrochim. Acta 40 (1995) 567–576.
[6] N.A. Vante, W. Jaegermann, H. Tributsch, W. Hoenle, K. Yvon, J. Am. Chem. Soc. 109 (1987) 3251–3257.
[7] A.A. Serov, S.-Y. Cho, S. Han, M. Min, G. Chai, K.H. Nam, C. Kwak, Electrochem. Commun. 9 (2007) 2041–2044.
[8] A.A. Serov, M. Min, G. Chai, S. Han, S. Kang, C. Kwak, J. Power Sources 175 (2008) 175–182.
[9] A. Serov, U. Tylus, K. Artyushkova, S. Mukerjee, P. Atanassov, Appl. Catal. B-Environ. 150–151 (2014) 179–186.
[10] J. Suntivich, H.A. Gasteiger, N. Yabuuchi, H. Nakanishi, J.B. Goodenough, Y. Shao-Horn, Nat. Chem. 3 (2011) 546–550.
[11] D.R. Rolison, Science 299 (2003) 1698–1701.
[12] J. Inukai, D. Cao, A. Wieckowski, K.-C. Chang, A. Menzel, V. Komanicky, H. You, J. Phys. Chem. C 111 (2007) 16889–16894.
[13] A. Zitolo, V. Goellner, V. Armel, M.-T. Sougrati, T. Mineva, L. Stievano, E. Fonda, F. Jaouen, Nat. Mater. 14 (2015) 937–942.
[14] K. Strickland, E. Miner, Q. Jia, U. Tylus, N. Ramaswamy, W. Liang, M.-T. Sougrati, F. Jaouen, S. Mukerjee, Nat. Commun. 6 (2015).
[15] V.S. Bagotzky, M.R. Tarasevich, K.A. Radyushkina, O.A. Levina, S.I. Andrusyova, J. Power Sources 2 (1978) 233–240.
[16] J.A.R. van Veen, H.A. Colijn, J.F. van Baar, Electrochim. Acta 33 (1988) 801–804.
[17] D.A. Scherson, S.L. Gupta, C. Fierro, E.B. Yeager, M.E. Kordesch, J. Eldridge, R. W. Hoffman, J. Blue, Electrochim. Acta 28 (1983) 1205–1209.
[18] S. Gupta, D. Tryk, I. Bae, W. Aldred, E. Yeager, J. Appl. Electrochem. 19 (1989) 19–27.
[19] A. Serov, K. Artyushkova, E. Niangar, C. Wang, N. Dale, F. Jaouen, M.-T. Sougrati, Q. Jia, S. Mukerjee, P. Atanassov, Nano Energy 16 (2015) 293–300.
[20] E. Proietti, F. Jaouen, M. Lefèvre, N. Larouche, J. Tian, J. Herranz, J.-P. Dodelet, Nat. Commun. 2 (2011) 416.
[21] Q. Jia, N. Ramaswamy, H. Hafiz, U. Tylus, K. Strickland, G. Wu, B. Barbiellini, A. Bansil, E.F. Holby, P. Zelenay, S. Mukerjee, ACS Nano 9 (2015) 12496–12505.
[22] N. Ramaswamy, U. Tylus, Q. Jia, S. Mukerjee, J. Am. Chem. Soc. 135 (2013) 15443–15449.
[23] U.I. Kramm, M. Lefèvre, N. Larouche, D. Schmeisser, J.-P. Dodelet, J. Am. Chem. Soc. 136 (2013) 978–985.
[24] U.I. Koslowski, I. Abs-Wurmbach, S. Fiechter, P. Bogdanoff, J. Phys. Chem. C 112 (2008) 15356–15366.
[25] U.I. Kramm, J. Herranz, N. Larouche, T.M. Arruda, M. Lefevre, F. Jaouen, P. Bogdanoff, S. Fiechter, I. Abs-Wurmbach, S. Mukerjee, J.-P. Dodelet, Phys. Chem. Chem. Phys. 14 (2012) 11673–11688.
[26] I.C. Stefan, Y. Mo, S.Y. Ha, S. Kim, D.A. Scherson, Inorg. Chem. 42 (2003) 4316–4321.
[27] A. Garsuch, A. Bonakdarpour, G. Liu, R. Yang, J.R. Dahn, in: W. Vielstich, H. Yokokawa, H.A. Gasteiger (Eds.), Handbook of Fuel Cells, New York, 2009, pp. 71–80.
[28] A. Serov, M.H. Robson, M. Smolnik, P. Atanassov, Electrochim. Acta 109 (2013) 433–439.
[29] A. Ohma, K. Shinohara, A. Iiyama, T. Yoshida, A. Daimaru, ECS Trans. 41 (2011) 775–784.
[30] U. Tylus, Q. Jia, K. Strickland, N. Ramaswamy, A. Serov, P. Atanassov, S. Mukerjee, J. Phys. Chem. C 118 (2014) 8999–9008.
[31] H. Schulenburg, S. Stankov, V. Schünemann, J. Radnik, I. Dorbandt, S. Fiechter, P. Bogdanoff, H. Tributsch, J. Phys. Chem. B 107 (2003) 9034–9041.
[32] K. Artyushkova, A. Serov, S. Rojas-Carbonell, P. Atanassov, J. Phys. Chem. C (2015).
[33] Y. Li, W. Zhou, H. Wang, L. Xie, Y. Liang, F. Wei, J.-C. Idrobo, S.J. Pennycook, H. Dai, Nat. Nano 7 (2012) 394–400.
[34] M.S. Thorum, J.M. Hankett, A.A. Gewirth, J. Phys. Chem. Lett. 2 (2011) 295–298.
[35] Y. Hu, J.O. Jensen, W. Zhang, L.N. Cleemann, W. Xing, N.J. Bjerrum, Q. Li, Angew. Chem. Int. Ed. 53 (2014) 3675–3679.
[36] D. Deng, L. Yu, X. Chen, G. Wang, L. Jin, X. Pan, J. Deng, G. Sun, X. Bao, Angew. Chem. Int. Ed. 52 (2013) 371–375.
[37] T.S. Olson, S. Pylypenko, J.E. Fulghum, P. Atanassov, J. Electrochem. Soc. 157 (2010) B54–B63.
[38] U.I. Kramm, I. Herrmann-Geppert, J. Behrends, K. Lips, S. Fiechter, P. Bogdanoff, J. Am. Chem. Soc. 138 (2016) 635–640.
[39] J.-P. Dodelet, R. Chenitz, L. Yang, M. Lefèvre, ChemCatChem 6 (2014) 1866–1867.
[40] D.Y. Chung, S.W. Jun, G. Yoon, S.G. Kwon, D.Y. Shin, P. Seo, J.M. Yoo, H. Shin, Y.-H. Chung, H. Kim, B.S. Mun, K.-S. Lee, N.-S. Lee, S.J. Yoo, D.-H. Lim, K. Kang, Y.-E. Sung, T. Hyeon, J. Am. Chem. Soc. 137 (2015) 15478–15485.
[41] M. Tavakkoli, T. Kallio, O. Reynaud, A.G. Nasibulin, C. Johans, J. Sainio, H. Jiang, E.I. Kauppinen, K. Laasonen, Angew. Chem. Int. Ed. 54 (2015) 4535–4538.
[42] D. Guo, R. Shibuya, C. Akiba, S. Saji, T. Kondo, J. Nakamura, Science 351 (2016) 361–365.
[43] S. Maldonado, K.J. Stevenson, J. Phys. Chem. B 108 (2004) 11375–11383.
[44] P.H. Matter, E. Wang, J.-M.M. Millet, U.S. Ozkan, J. Phys. Chem. C 111 (2007) 1444–1450.
[45] B. Winther-Jensen, O. Winther-Jensen, M. Forsyth, D.R. MacFarlane, Science 321 (2008) 671–674.
[46] K. Gong, F. Du, Z. Xia, M. Durstock, L. Dai, Science 323 (2009) 760–764.
[47] M. Pumera, H. Iwai, Chem. – Asian J. 4 (2009) 554–560.
[48] J. Masa, A. Zhao, W. Xia, Z. Sun, B. Mei, M. Muhler, W. Schuhmann, Electrochem. Commun. 34 (2013) 113–116.
[49] J. Masa, A. Zhao, W. Xia, M. Muhler, W. Schuhmann, Electrochim. Acta 128 (2014) 271–278.
[50] J. Masa, W. Xia, M. Muhler, W. Schuhmann, Angew. Chem. Int. Ed. 54 (2015) 10102–10120.
[51] M.W. Louie, A.T. Bell, J. Am. Chem. Soc. 135 (2013) 12329–12337.
[52] L. Birry, J.H. Zagal, J.-P. Dodelet, Electrochem. Commun. 12 (2010) 628–631.
[53] U.I. Kramm, I. Abs-Wurmbach, I. Herrmann-Geppert, J. Radnik, S. Fiechter, P. Bogdanoff, J. Electrochem. Soc. 158 (2011) B69–B78.
[54] P.H. Matter, E. Wang, M. Arias, E.J. Biddinger, U.S. Ozkan, J. Mol. Catal. A: Chem. 264 (2007) 73–81.
[55] G. Wu, M.A. Nelson, N.H. Mack, S. Ma, P. Sekhar, F.H. Garzon, P. Zelenay, Chem. Commun. 46 (2010) 7489–7491.
[56] K. Artyushkova, A. Serov, S. Rojas-Carbonell, P. Atanassov, J. Phys. Chem. C 119 (2015) 25917–25928.
[57] S. Kabir, K. Artyushkova, B. Kiefer, P. Atanassov, Phys. Chem. Chem. Phys. 17 (2015) 17785–17789.
[58] M. Ferrandon, A.J. Kropf, D.J. Myers, K. Artyushkova, U. Kramm, P. Bogdanoff, G. Wu, C.M. Johnston, P. Zelenay, J. Phys. Chem. C 116 (2012) 16001–16013.
[59] E.F. Holby, C.D. Taylor, Sci. Rep. 5 (2015).
[60] E. Proietti, F. Jaouen, M. Lefèvre, N. Larouche, J. Tian, J. Herranz, J.-P. Dodelet, Nat. Commun. 2 (2011) 416.
[61] A.L. Bouwkamp-Wijnoltz, W. Visscher, J.A.R. van Veen, Electrochim. Acta 43 (1998) 3141–3152.
[62] T. Okada, M. Gokita, M. Yuasa, I. Sekine, J. Electrochem. Soc. 145 (1998) 815–822.
[63] J.D. Wiggins-Camacho, K.J. Stevenson, J. Phys. Chem. C 115 (2011) 20002–20010.
[64] C. Gumeci, N. Leonard, Y. Liu, S. McKinney, B. Halevi, S.C. Barton, J. Mater. Chem. A 3 (2015) 21494–21500.
[65] A.L. Bouwkamp-Wijnoltz, W. Visscher, J.A.R. van Veen, E. Boellaard, A.M. van der Kraan, S.C. Tang, J. Phys. Chem. B 106 (2002) 12993–13001.
[66] S. Kim, D. Tryk, I.T. Bae, M. Sandifer, R. Carr, M.R. Antonio, D.A. Scherson, J. Phys. Chem. 99 (1995) 10359–10364.
[67] S. Kuroki, Y. Nabae, M.-a Kakimoto, S. Miyata, ECS Trans. 41 (2011) 2269–2276.
[68] G. Wu, C.M. Johnston, N.H. Mack, K. Artyushkova, M. Ferrandon, M. Nelson, J. S. Lezama-Pacheco, S.D. Conradson, K.L. More, D.J. Myers, P. Zelenay, J. Mater. Chem. 21 (2011) 11392–11405.
[69] G. Wu, Z. Chen, K. Artyushkova, F.H. Garzon, P. Zelenay, ECS Trans. 16 (2008) 159–170.
[70] M. Lefèvre, J.P. Dodelet, P. Bertrand, J. Phys. Chem. B 109 (2005) 16718–16724.
[71] M. Lefèvre, J.P. Dodelet, P. Bertrand, J. Phys. Chem. B 106 (2002) 8705–8713.
[72] S.L. Gojković, S. Gupta, R.F. Savinell, J. Electrochem. Soc. 145 (1998) 3493–3499.
[73] M. Bron, J. Radnik, M. Fieber-Erdmann, P. Bogdanoff, S. Fiechter, J. Electroanal. Chem. 535 (2002) 113–119.
[74] Q. Jia, J. Li, K. Caldwell, D.E. Ramaker, J.M. Ziegelbauer, R.S. Kukreja, A. Kongkanand, S. Mukerjee, ACS Catal. 6 (2016) 928–938.
[75] I.T. Bae, D.A. Tryk, D.A. Scherson, J. Phys. Chem. B 102 (1998) 4114–4117.
[76] D.A. Scherson, S.B. Yao, E.B. Yeager, J. Eldridge, M.E. Kordesch, R.W. Hoffman, J. Phys. Chem. 87 (1983) 932–943.
[77] A. Serov, M.H. Robson, M. Smolnik, P. Atanassov, Electrochim. Acta 80 (2012) 213–218.
[78] A. Serov, M.H. Robson, B. Halevi, K. Artyushkova, P. Atanassov, Electrochem. Commun. 22 (2012) 53–56.
[79] M.H. Robson, A. Serov, K. Artyushkova, P. Atanassov, Electrochim. Acta 90 (2013) 656–665.
[80] A. Serov, K. Artyushkova, N.I. Andersen, S. Stariha, P. Atanassov, Electrochim. Acta 179 (2015) 154–160.
[81] M.C.M. Alves, J.P. Dodelet, D. Guay, M. Ladouceur, G. Tourillon, J. Phys. Chem. 96 (1992) 10898–10905.
[82] C.H. Choi, C. Baldizzone, J.-P. Grote, A.K. Schuppert, F. Jaouen, K.J.J. Mayrhofer, Angew. Chem. Int. Ed. 54 (2015) 12753–12757.
[83] G. Zhang, R. Chenitz, M. Lefèvre, S. Sun, J.-P. Dodelet, Nano Energy (2016), http://dx.doi.org/10.1016/j.nanoen.2016.02.038.
[84] N.R. Sahraie, U.I. Kramm, J. Steinberg, Y. Zhang, A. Thomas, T. Reier, J.-P. Paraknowitsch, P. Strasser, Nat. Commun. 6 (2015).
[85] F. Jaouen, J.-P. Dodelet, Electrochim. Acta 52 (2007) 5975–5984.
[86] S. Ma, G.A. Goenaga, A.V. Call, D.-J. Liu, Chem. – Eur. J. 17 (2011) 2063–2067.
[87] N.D. Leonard, K. Artyushkova, B. Halevi, A. Serov, P. Atanassov, S.C. Barton, J. Electrochem. Soc. 162 (2015) F1253–F1261.

[88] G. Wu, A. Santandreu, W. Kellogg, S. Gupta, O. Ogoke, H. Zhang, H.-L. Wang, L. Dai, Nano Energy (2016), http://dx.doi.org/10.1016/j.nanoen.2015.12.032.
[89] S. Mukerjee, Development of Novel Non-Pt Group Metal Electrocatalysts for Proton Exchange Membrane Fuel Cell Applications, 2015 ⟨https://www.hydrogen.energy.gov/pdfs/review15/fc086_mukerjee_2015_o.pdf⟩.
[90] L. Fan, P.F. Liu, X. Yan, L. Gu, Z.Z. Yang, H.G. Yang, S. Qiu, X. Yao, Nat. Commun. 7 (2016).
[91] H. Fei, J. Dong, M.J. Arellano-Jiménez, G. Ye, N.D. Kim, E.L. Samuel, Z. Peng, Z. Zhu, F. Qin, J. Bao, Nat. Commun. 6 (2015).
[92] M. Tavakkoli, T. Kallio, O. Reynaud, A.G. Nasibulin, C. Johans, J. Sainio, H. Jiang, E.I. Kauppinen, K. Laasonen, Angew. Chem. 127 (2015) 4618–4621.
[93] J. Deng, P. Ren, D. Deng, L. Yu, F. Yang, X. Bao, Energy Environ. Sci. 7 (2014) 1919–1923.

Dr. Qingying Jia (M.S. and B.S. in Physics from Beijing University) is currently a Research Assistant Professor at Northeastern University. He obtained his Ph.D. in Material Sciences at Illinois Institute of Technology, USA in 2010. His research centers on synchrotron-based in situ X-ray absorption spectroscopy (XAS) characterization of (electro)catalysts with applications to fuel cells and batteries.

Dr. Nagappan Ramaswamy is currently a Research Engineer at the Global Fuel Cell Activities Division, General Motors Corporation located at Pontiac, Michigan USA. He received a Bachelor of Chemical & Electrochemical Engineering degree from Central Electrochemical Research Institute, India in 2005 and a Ph.D. degree in Physical Chemistry from Northeastern University, USA in 2011. His doctoral thesis involved the investigation of precious and non-precious electrocatalyst materials in acid and alkaline electrolytes with a particular emphasis on unraveling the fundamental relationships between electrochemical double layer structure and catalytic mechanisms.

Dr. Urszula Tylus obtained her Ph.D. in Chemistry at Northeastern University, Boston, MA under advisory of Prof. Sanjeev Mukerjee and a Masters degree in Chemical Technology (Kraków University of Technology, Kraków, Poland). Her research experience includes postdoctoral work in Los Alamos National Laboratory under mentorship of Dr. Piotr Zelenay and several years of earlier work in industrial Research and Development (W.R. Grace, Cambridge, MA). Urszula's doctoral and postdoctoral research focused on synthesis and fundamental investigations of non-precious metal based catalysts for applications in fuel cells and electrolyzers using synchrotron-based in situ X-ray absorption spectroscopy (XAS).

Dr. Kara Strickland is currently teaching Physics at Mystic Valley Regional Charter School in Malden, MA. She obtained her Ph.D. in Chemistry at Northeastern University in 2015. Her research focuses on development and characterization of electrocatalyst for fuel cells and electrolyzers, with an emphasis on characterization with synchrotron-based in situ X-ray absorption spectroscopy (XAS).

Miss Jingkun Li received her Bachelor degree in Applied Chemistry from Hefei University of Technology in 2009 and Master degree in Chemical Engineering from Shanghai Jiao Tong University in 2012 under the advisory of Prof. Zifeng Ma. She is currently pursuing her Ph.D. degree under the supervision of Prof. Sanjeev Mukerjee at Northeastern University focusing on oxygen reduction reaction.

Alexey Serov (M.S. in Inorganic Chemistry from Moscow State University, and Ph.D. in Physical Chemistry from University of Bern) is a Research Associate Professor of Chemical & Biological Engineering Department at the University of New Mexico. His research focuses on materials design and characterization for energy applications and includes development of electrocatalyst for fuel cells, electrolyzers and lithium-ion batteries. He is the author of more than 60 peer-reviewed articles and 65 issued patents (USA and international).

Dr. Kateryna Artyushkova obtained her Ph.D. at the Chemistry Department, Kent State University, Kent, Ohio, in 2001 under the supervision of Professor Julia E. Fulghum. She was a post-doctoral scientist at Chemical and Nuclear Engineering Department at University of New Mexico, focusing on multivariate analysis of spectroscopic and imaging data, image fusion and digital image processing. In 2008, Kateryna Artyushkova has been promoted to research Associate Professor at UNM. She has more than 15 years of experience with all aspects of X-ray photoelectron spectroscopy, including instrumentation, experimental design for optimizing time and information content, and data analysis. Her research focuses on developing methodology for accelerating material design through structure-to-property modeling and characterization of functional materials using ex-situ and in-situ spectroscopic and microscopic techniques.

Plamen Atanassov (M.S. in Chemical Physics from University of Sofia, and Ph.D. in Physical Chemistry from the Bulgarian Academy of Sciences) is a Distinguished Professor of Chemical & Biological Engineering and Chemistry & Chemical Biology at the University of New Mexico. He is the director of the Center for Micro-Engineered Materials. His research focuses on electrocatalysis and bio-electrocatalysis and includes development of electrocatalyst for fuel cells, new materials and technologies for energy conversion and harvesting such as biological fuel cells, enzymatic and microbial as well as sensors design and integration.

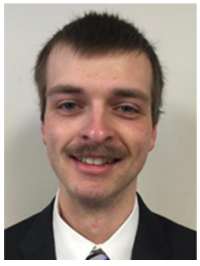

Jacob Anibal is a 2016 graduate of Michigan State University with a B.S. in Chemical Engineering. He will begin his doctoral degree program in Fall 2016.

Cenk Gumeci, obtained his Ph.D. at Texas Tech University, Department of Chemistry, under the direction of Prof. Carol Korzeniewski in 2014. He worked as a postdoctoral researcher at Michigan State University with Prof. Scott Calabrese Barton for a year. He then joined to Nissan Technical Center North America (NTCNA) as a Research Associate for fuel cell research. His research interests involve noble and non-noble nanomaterial synthesis and characterization for proton exchange membrane fuel cells, super capacitors and batteries. He is the author of more than 10 peer-reviewed articles.

Scott Calabrese Barton is an Associate Professor of Chemical Engineering at Michigan State University. He completed his Ph.D. in Chemical Engineering at Columbia University in 1999 after studying Aerospace Engineering at the University of Notre Dame and Massachusetts Institute of Technology. Prior to joining MSU in 2006, he worked as a postdoctoral associate at the University of Texas and as Assistant Professor at Columbia University. His work has covered a range of electrochemical systems, including direct methanol fuel cells, zinc-air batteries, biofuel cell electrodes and platinum-free catalysts for oxygen reduction.

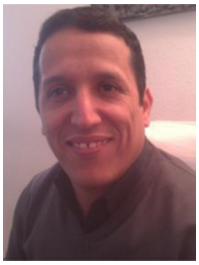

Dr. Moulay Tahar Sougrati is a CNRS Research Engineer in charge of the Mössbauer spectroscopy platform of the Charles Gerhardt Institute. He focuses on the characterization with Mössbauer spectroscopy of novel materials for energy storage and conversion. He carried out his Ph. D. on the application of ^{119}Sn Mössbauer spectroscopy to study the atmospheric corrosion of Sn-based materials (GPM, Rouen). He then moved to Liège University (2007, 2009) where he applied ^{57}Fe Mössbauer spectroscopy to characterize metallic, organometallic and inorganic materials. Since 2009, he is involved in both the European (ALISTORE-ERI) and the French (RS2E) networks for electrochemical energy storage.

Dr. Frédéric Jaouen obtained his Ph.D. at the Royal Institute of Technology, Stockholm, in 2003 under supervision of Prof. Lindbergh. He was then a research associate in Professor Dodelet's group, Canada, where he focused on non-precious metal catalysts for oxygen reduction. In 2011, Frédéric Jaouen was awarded an excellence chair from the Agence Nationale de la Recherche and moved to Université de Montpellier, France, to pursue his research on novel catalysts for electrochemical energy conversion as a CNRS research fellow. His current interests are the development of catalysts and complete cells based on Earth-abundant elements and the elucidation of structure–property relationships.

Dr. Barr Halevi obtained his Ph.D. in Chemical and Biomolecular Engineering at the University of Pennsylvania in 2008 under the supervision of Profs. John M. Vohs and Raymond J. Gorte. He was a post-doctoral scholar in the department of Chemical and Nuclear Engineering at the University of New Mexico, and worked with Profs. Abhaya K. Datye and Plamen Atanassov where he developed model catalysts for low temperature reforming and catalysts for low temperature Anion-Exchange Fuel Cells. In 2012 he helped found Pajarito Powder, a company focused on commercializing low-cost fuel cell catalysts.

Dr. Sanjeev Mukerjee is a Professor in the Department of Chemistry and Chemical Biology (Northeastern University); where he has been since September of 1998. He also heads the newly created center for Renewable Energy Technology and its subset the Laboratory for Electrochemical Advanced Power (LEAP).He is the author of 130 peer-reviewed publications with a current H-index of 53 and is a fellow of the Electrochemical Society. He has given numerous invited and keynote presentations in various national and international meetings and holds five US and international patents. He also serves on the scientific advisory boards of three companies.